Journal Name

ARTICLE TYPE

Cite this: DOI: 10.1039/xxxxxxxxxx

Mechanistic Insights into Hydrodeoxygenation of Phenol on Bimetallic Phosphide Catalysts†

Varsha Jain,[a] Yolanda Bonita,[b] Alicia Brown,[a‡] Anna Taconi,[a‡] Jason C. Hicks,[b] and Neeraj Rai[a*]

Received Date
Accepted Date

DOI: 10.1039/xxxxxxxxxx

www.rsc.org/journalname

Catalytic hydrodeoxygenation (HDO) of phenolics is a necessary step for upgrading bio-oils to transportation fuels. Bimetallic catalysts offer the potential of increased activities and selectivities for desired products. Adding non-metallic elements, such as phosphorous, allows for charge distribution between the metal and nonmetal atoms, which improves Lewis acid character of catalytic surfaces. This work utilizes experimental and density functional theory (DFT) based calculations to identify potential C–O bond cleavage pathways and product selectivity for HDO reactions on FeMoP, RuMoP, and NiMoP catalysts. Our work demonstrates that FeMoP catalyst favors direct deoxygenation pathway due to a lower activation energy barrier for C–O bond cleavage whereas RuMoP and NiMoP catalysts promote ring hydrogenation first, followed by the cleavage of C–O bond. The Bader charge analysis indicates that for these catalytic systems $Mo^{\delta+}$ site bears a large positive charge which acts as a Lewis acid site for HDO reactions. Overall, we find that trends in the experimental product selectivities are in good agreement with that predicted with DFT calculations.

1 Introduction

Due to increasing demand for energy resources, new technologies are desired for the conversion of biomass, which is a renewable carbon source, to valuable chemicals and fuels.[1–7] Bio-oil is a by-product of biomass during pyrolysis process which contains around 20-50 wt% oxygen in the form of heterocyclic rings, aromatic alcohols, hydroxycarbonyl compounds, carboxylic acids, anhydrosugars, and larger fragments of lignocellulosic polymers.[8–11] These oxygen-containing compounds cause chemical instability, poor volatility, high viscosity, corrosiveness, and low heating value of bio-oil.[12,13] The production of bio-oil from biomass can be relatively cheap and efficient, but the presence of oxygen poses a significant challenge that must be overcome before utilization of bio-oil as a transportation fuel.[10,14,15] The process of removing oxygen in the form of water broadly termed by hydrodeoxygenation (HDO) and phenol is often adopted as the simplest bio-oil product to investigate HDO reaction mechanisms.[16–24]

HDO of phenolic compounds is believed to occur via two routes.[20,22,23] The first route is the direct deoxygenation (DDO) pathway where in the presence of H_2, direct cleavage or hydrogenolysis of the C–O bond occurs while the aromatic ring is preserved. The second route involves ring hydrogenation (RH) in the presence of H_2, followed by hydrogenolysis (RH-DO) or dehydration (RH-DEHYD). In the case of phenol HDO, the DDO pathway produces benzene, while the RH-DO or RH-DEHYD pathway produces ring hydrogenated products such as cyclohexanol, cyclohexene, and cyclohexane.[20,22,23,25,26] For these two HDO routes, two kinds of active sites are required, namely one site that could split H_2, and the other that could adsorb the phenolics. During these HDO reactions, the adsorption of phenyl ring on the catalytic surface due to the π electron cloud would probably lead to the hydrogenated phenyl ring whereas the adsorption through phenolic hydroxyl group would yield benzene. As DDO reaction requires cleavage of strong C-O bonds directly, it is sometimes strategic to weaken the C-O bond first via ring hydrogenation and then proceed hydrogenolysis or dehydration reaction for

[a] Dave C. Swalm School of Chemical Engineering and Center for Advanced Vehicular Systems, Mississippi State University, Mississippi State, Mississippi 39762, United States.
[b] Department of Chemical and Biomolecular Engineering, 182 Fitzpatrick Hall, University of Notre Dame, Indiana 46556, United States.
‡ Authors AB and AT contributed equally.
* E-mail: neerajrai@che.msstate.edu; Tel: (+1) 662-325-0790; Fax: (+1) 662-325-2482.

† Electronic Supplementary Information (ESI) available: [lattice vectors (Table S1), effect of k-point sampling on adsorption energies and activation energies (Table S2), effect of grid size on Bader charges (Table S3), lattice parameters (Table S4), adsorption energies (Table S5, S6, and S8), partial charges (Table S3 and S10), distances (Table S7), activation energies (Table S2, S9, S11, and S12), XRD pattern (Fig. S1), optimized structure of phenol on (111) facet of NiMoP (Fig. S2), reaction energetics (Fig. S3 and S6), DDO reaction on the (112) facets of RuMoP and NiMoP catalyst (Fig. S4 and S5), and atom numbering for Table S6 (Fig. S7)]. See DOI: 10.1039/x0xx00000x

C-O σ bond cleavage.[27,28] However, RH-DO or RH-DEHYD route requires more H_2 in comparison to the DDO route and is thus less economical. To examine reaction mechanisms on specific catalytic surface, in the past, many studies have been done on HDO of bio fuel model compounds by using supported or unsupported catalysts such as sulfided metals (i.e. Mo, Ni, Co),[29,30] zeolites,[31,32] noble metal catalysts,[33–38] and metal carbides,[39–41] nitrides,[41] phosphides,[41–54] borides,[55,56] and oxides[41,57]. This work is focused on HDO using metal phosphides due to their high activity and selectivity towards C-O scission in HDO reactions.[58]

Monometallic phosphide catalysts using metals such as Co, Ni, Mo, Fe, Ru, and W have received great attention due to their deoxygenation ability.[41–50,59] However, the catalytic properties can be altered further by the incorporation of a second metal to form bimetallic phosphides. For example, guaiacol HDO with monometallic MoP and Fe_2P resulted in 43 and 63 % selectivity, respectively, towards the direct deoxygenation products.[51] However, when a solid solution of FeMoP was tested for the same reaction, the selectivity increases to 78 %. Higher direct deoxygenation selectivity of 90 % was later reported for FeMoP for phenol HDO.[51–54] An increase in direct deoxygenation selectivity was also observed when Mo was incorporated into Ni phosphide for anisole HDO.[42] It was evident that metal incorporation to form bimetallic phosphides could alter the catalytic properties of the material due to the change in surface electronic structure, electron density, and bi-functional character of these materials.[17,42,60–64]

In our previous work, we have shown that the product selectivity of phenol HDO can be controlled by changing the composition in $Fe_XMo_{2-X}P$.[53] The electronic structure analysis showed that the direct deoxygenation selectivity was highly dependent on the interaction between the metal in bimetallic phosphide and the oxygen atom in phenol. A recent experimental study on a series of bimetallic phosphides MMoP (M = Fe, Co, Ni) showed a significantly different catalytic activity towards ring hydrogenation and direct deoxygenation products.[53,54] Although experimental techniques alluded to Mo oxidation state as a key descriptor, a molecular level understanding is necessary to develop periodic trends in the catalytic activity of these Mo-based bimetallic phosphides. In this work, we focus on FeMoP, RuMoP, and NiMoP bimetallic phosphides as these were previously reported to show distinct product selectivity for phenol HDO.[54] We use DFT to develop a mechanistic understanding of HDO of phenol on these catalysts and to rationalize selectivity observed in the experiments.

2 Methods

2.1 Computational approach

We performed plane wave periodic density functional theory[65,66] calculations using Vienna *ab initio* simulation package (VASP.5.4.1).[67–70] We have used the optB88-vdW functional[71,72] to better describe nonlocal van der Waals interactions. The core electrons are described with the projector augmented wave (PAW) method[73] to solve the Kohn-Sham equations.[74,75] The energy cut-off was taken as 450 eV to ensure high precision. Total energies were calculated using a first-order Methfessel−Paxton smearing function with a width of 0.1 eV,[76] and the total energy was extrapolated to 0 K. Optimizations were carried out until the net forces acting on atoms were smaller than 0.03 eV $Å^{-1}$, using a total energy convergence of 1 x 10^{-5}eV. Spin polarization had an appreciable effect on the overall energies; for example, the total energies are different by 0.005 eV for adsorbed phenol on FeMoP, RuMoP, and NiMoP surface. The calculations were, therefore, carried out with spin polarization. For the integration of the Brillouin zone (BZ), we have used Γ-point sampling as the supercells are sufficiently large (see Table S1).[77] To see the effect of k-point sampling, calculations were performed with a grid of 2 X 2 X 1 and 4 X 4 X 1. The activation energy barriers for C–O bond cleavage obtained for Γ-point, 2 X 2 X 1, and 4 X 4 X 1 grids were virtually identical with differences $\leq \sim 0.003$ eV (see Table S2). Due to the minor differences in the energy, we performed all calculations with only Γ-point sampling to reduce the computational cost. The partial charges on various species were determined using Bader charge analysis.[78–81] We checked the convergence of Bader charges with respect to the FFT grid density and found that doubling the number of grid points had only marginal effect (partial atomic charges changed by less than 0.03 e). (see Table S3).

The unit cell of bulk FeMoP, NiMoP, and RuMoP was built based on experimental work (Fig. S1), which was then optimized under three-dimensional periodic boundary conditions to further refine the structure using DFT.[53,54] The optimized unit cell parameters differed ≤ 2 % when compared to the experimentally determined cell parameters (Table S4). Using these optimized cell parameters, the model phosphide surface was constructed by implementing the standard slab approach, in which a slab of finite thickness was cut out of the FeMoP, RuMoP and NiMoP crystal at the (112) plane to expose an atomic layer that has all three types of atoms for each catalytic surface. Recently published article by Bonita et al. and X-ray diffraction (XRD) pattern in Fig. S1 prove that for FeMoP and RuMoP catalyst, (112) plane is the most dominant plane, and for NiMoP catalyst (111) plane is the dominant facet.[54] Thus, we have also performed the same HDO reaction mechanisms on (111) NiMoP plane which is shown in additional supplementary information (SI).

The unit cell of FeMoP and RuMoP has an orthorhombic crystallographic structure, whereas NiMoP has a hexagonal crystallographic structure. The slabs used for simulations consist of three, three, and four layers in FeMoP, RuMoP, and NiMoP, respectively, with a supercell size *P (2* X *2)* with a 15 Å thick vacuum layer in the z-direction (perpendicular to the surface) to minimize interactions between neighboring image slabs. However, to see the effect of simulation cell size on the adsorption energies, we performed simulations on *P (4* X *4)* cell size of each system and found that adsorption energies change by $\leq \sim 0.007$ eV (see Table S5). The number of layers are different to keep the total number of atoms same, as well as to maintain 1:1:1 (M = Fe, Ru, Ni:Mo:P) composition of all kinds of atoms in a system. Throughout the calculations, the one, one, and two bottom-most layers of the slabs were fixed to represent the corresponding crystal structure for FeMoP, RuMoP, and NiMoP, respectively, whereas all other atoms in the systems were relaxed. The number of slab layers were

tested by increasing the substrate to four, four, and five layers (bottom two, two, and three fixed for FeMoP, RuMoP, and NiMoP, respectively) for FeMoP, RuMoP, and NiMoP, respectively, to perform hydrodeoxygenation of phenolic compounds and was found the change in adsorption energy by only ~ 0.003 eV. Phenol was chosen as a model surrogate molecule from phenolic compounds.

The adsorption energies (denoted as E_{AD}) were calculated according to Eqn. (1), wherein $E_{ADSORBATE+SURFACE}$ is defined as the total energy of species adsorbed on the surface; $E_{SURFACE}$ is defined the total energy of surface; and $E_{ADSORBATE}$ is defined as the energy of the adsorbed species on the surface in the gas phase.

$$E_{AD} = E_{ADSORBATE+SURFACE} - E_{SURFACE} - E_{ADSORBATE} \quad (1)$$

Transition states for the elementary steps in the chemical transformation were identified using the nudged elastic band (NEB) method[82–84], and these were further refined with the climbing image nudged elastic band (CINEB) method.[85] Transition states were confirmed by examining vibrational frequencies (presence of only one imaginary frequency). The activation energy barrier (denoted as E_A) with respect to each transition energy state (E_{TS}) was calculated by Eqn. (2), where E_R denotes the total energy of reactant.

$$E_A = E_{TS} - E_R \quad (2)$$

Since our goal is to compare the mechanistic pathways (rather than the absolute rates) on the surface of the catalysts with different metal compositions, we only considered electronic energies and the thermal and coverage effects were not included.

2.2 Catalyst preparation

Unsupported bimetallic phosphides were synthesized using a temperature programmed reduction (TPR) method as described in previous work.[51–53] To 50 mL of deionized water, 0.7 mmol of citric acid (Amresco) was added followed by 0.5 mmol of $(NH_4)_6Mo_7O_{24}{\cdot}4H_2O$ (Alfa Aesar), 0.5 mmol of second metal salt ($FeNO_3{\cdot}9H_2O$, Alfa Aesar; $NiNO_3{\cdot}6H_2O$, Alfa Aesar; or $RuCl_3{\cdot}xH_2O$, Strem Chemicals), and 0.5 mmol of $(NH_4)_2HPO_4$ (Amresco). The volume of the solution was reduced by 50 % using a rotovap, and the resulting slurry was calcined at 550 °C for 6 h with a 1 °C/min ramp rate. After calcination, the powder was finely ground with a mortar and pestle and subsequently reduced with a 99.999 % H_2 (Airgas) stream at 160 mL/min and 650 °C for 2 h using a 5 °C/min ramp rate. The final powder was passivated in 1 % O_2/He (Airgas) for 1 h and transferred to a N_2 glove box.

2.3 Characterization

The crystal structures of the phosphide catalysts were confirmed using X-ray diffraction (XRD) with a Bruker DaVinci Advanced D8 powder X-ray diffractometer. The bulk oxidation of the materials was analyzed using X-ray absorption near edge structure (XANES) spectroscopy at the advanced photon source (APS) in Argonne National Laboratory. The experiment was performed in sector 10 insertion device (ID) beamline of the Material Research Collaborative Access Team (MRCAT). The samples were diluted with boron nitride and packed into a sample holder before pretreatment. The samples were then pretreated with a stream of 4 % H_2/He at 400 °C for 1 hr. WinXAS was used to analyze the XANES data.

2.4 Catalytic reactions

The catalytic performance of the materials was tested in a 1/4 inch outside diameter, stainless steel flow reactor. The reactor was packed with 50.0 mg of SiO_2, 120.0 mg of SiO_2 mixed with 30.0 mg of catalysts, 25.0 mg of SiO_2, and 10.0 mg of quartz wool (in order from top to bottom of the reactor). The catalyst was pretreated with a 100 mL/min H_2 stream at 400 °C for 1 h prior to reaction. After pressurizing to 600 psig, the liquid feed containing 0.10 M phenol in decane was pumped into the reactor using a Hitachi L-6000 pump at flow rates varied between 1.2−0.3 mL/min. The products and residual reactants in the effluent stream were quantified using an Agilent 7890 gas chromatograph (GC) equipped with an Agilent 5975 mass spectroscopy (MS). Concentrations of species were determined from external calibration curves.

3 Results and discussion

Bimetallic phosphide catalysts exhibit a wide range of surface chemistry, thus, can promote different reaction pathways for transforming phenol to the deoxygenated molecules. To understand the trends in catalytic activity, this work determines the effect of changing the second metal (Fe, Ru, Ni), apart from Mo, in bimetallic phosphide catalyst to understand HDO reaction pathways which are shown in Fig. 1. The purpose of DFT calculations is to better understand the mechanistic role of surface Lewis acidity in these catalysts in directing turnover frequencies (TOFs) for C–O bond cleavage of phenol.

3.1 Charge distribution in the catalyst using Bader analysis and XANES

The addition of nonmetals such as phosphorus in a bimetallic system can lead to a significant redistribution of electronic charge density due to differences in the electronegativity of transition metal and non-metal elements. The charge transfer leads to electron rich and electron deficient sites on the catalytic surface. The electron deficient sites can potentially act as Lewis acid sites and tend to correlate with the number of Lewis acid sites available on catalytic surfaces. We found average total positive partial charge on FeMoP and RuMoP catalytic surface is +0.81 |e| and +0.78 |e|, respectively, whereas it is +0.64 |e| for NiMoP catalytic surface (see Table 1). The total positive charge is localized primarily on Mo sites whereas the P sites are electron rich. The comparison between the partial atomic charges on the elements in the bulk and on the surface suggests that atoms on the surface experience greater charge transfer (see Table 1).

We performed XANES experiments to further understand the charge distribution on the catalytic surface. XANES is a powerful tool to probe the nature of the electronic structure of the surface

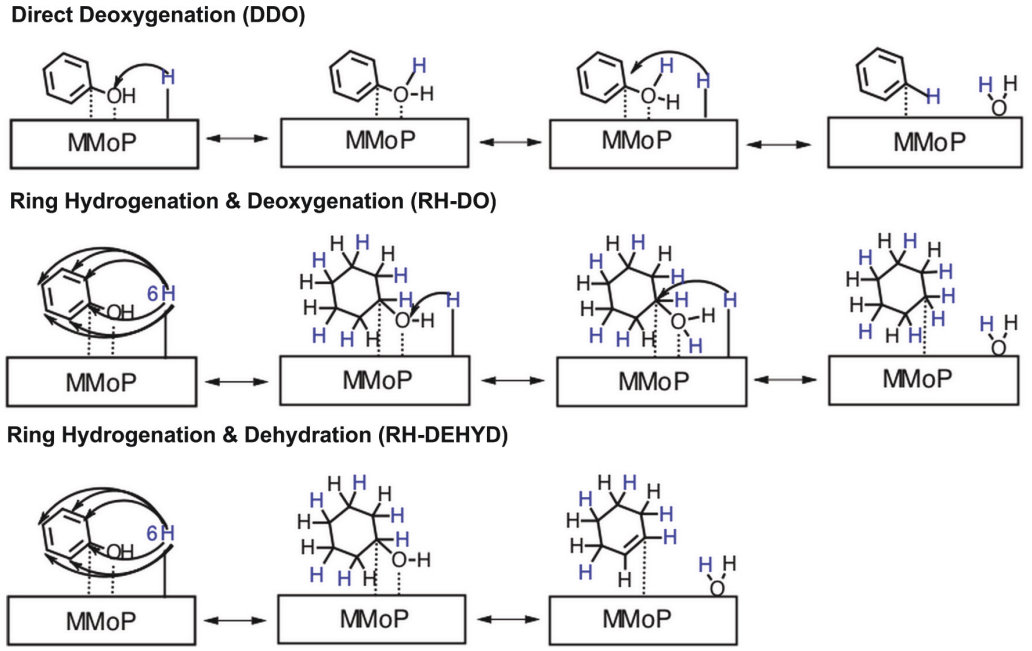

Fig. 1 Different hydrodeoxygenation (HDO) reaction mechanisms for phenol (C_6H_5OH) on bimetallic phosphide catalysts (M = Fe, Ru, Ni).

Table 1 Average partial atomic charge (q, |e|) of each type of surface atom on (112) facet and in the bulk of FeMoP, RuMoP, and NiMoP catalysts

system	atom	$q_{surface}$	q_{bulk}
FeMoP	Fe	+0.07	+0.09
	Mo	+0.74	+0.65
	P	– 0.81	– 0.74
RuMoP	Ru	– 0.23	– 0.24
	Mo	+0.78	+0.61
	P	– 0.55	– 0.37
NiMoP	Ni	+0.01	– 0.05
	Mo	+0.63	+0.65
	P	– 0.64	– 0.60

as shown in literature.[86–89] We recently reported the use of both X-ray photoelectron spectroscopy (XPS) and XANES to probe the nature of Mo in various bimetallic phosphides such as FeMoP, NiMoP, RuMoP, and CoMoP.[54] These results provided evidence that Mo in the MMoP (M = Fe, Ni, Ru, and Co) solid solutions is relatively oxidized compared to Mo^0 and is a potential descriptor for catalyst performance in phenol hydrodeoxygenation reactions.[54] Here, we report the results of XANES experiments on the non-Mo metal (e,g., Fe, Ru, or Ni) in the bimetallic MMoP catalysts. The XANES data were obtained with a standard reduced metal foil that acted as a reference with reference value of 7112.0, 8332.8, and 22117.2 eV for Fe, Ni, and Ru, respectively. The shifted and normalized K-edge XANES data of Fe, Ni, and Ru were plotted in Fig. 2 (a), Fig. 2 (b), and Fig. 2 (c), respectively with the appropriate photon energy scale for each spectrum since they differ in absorption energy. The absorption energy in this analysis is defined as the first inflection point (1s→4p transition) after the pre-edge spectrum. The absorption energy shifts of Fe, Ru, and Ni in bimetallic Mo-based phosphides were found to be 1.5, 1.0, and 1.2 eV higher compared to their reduced form M^0. The results suggested that these metals are also slightly oxidized. Attempts to assign a formal oxidation state to these metals failed as these shifts are not significant enough for metal oxides. For example, the shift of Fe^{3+} is 11.9 eV, Ru^{3+} is 10.6 eV, and Ni^{2+} is 19.2 eV.[90–92]

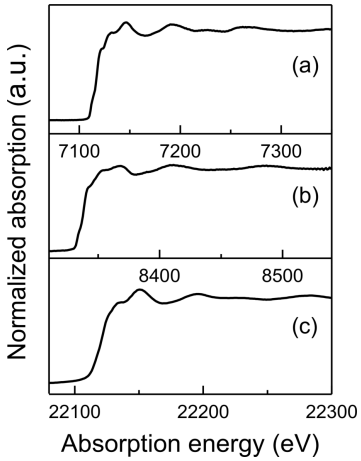

Fig. 2 Normalized XANES of (a) Fe K-edge of FeMoP (b) Ni K-edge of NiMoP (c) Ru K-edge of RuMoP.

Overall, the XANES results provided insight into the relative oxidation of the metals and according to that, all of the metals were found to be positively charged as a result of charge transfer with the anionic P atom.[54] The experimental measurement agreed with the Bader charge calculation except for the Ru atom. The Bader charge analysis showed that the Ru was negatively charged with -0.23 |e|, while the XANES result showed that Ru was positively charged. The result was interesting since the calculation suggested Ru as an electron acceptor, while the experimental measurement suggested otherwise. It is important

Table 2 Adsorption energies (E_{AD}, eV) of phenol(C_6H_5OH), benzene (C_6H_6), cyclohexanol ($C_6H_{11}OH$), cyclohexene (C_6H_{10}), and cyclohexane (C_6H_{12}) on (112) facet of FeMoP, RuMoP, and NiMoP catalyst for different DFT functionals

molecule	FeMoP		RuMoP		NiMoP	
	optB88-vdW	PW91	optB88-vdW	PW91	optB88-vdW	PW91
phenol	-1.39	-1.37	-1.29	-1.21	-1.21	-1.1
benzene	-1.73	-1.68	-1.53	-1.42	-1.27	-1.18
cyclohexanol	-1.05	-1.04	-1.13	-1.12	-1.17	-1.15
cyclohexene	-0.97	-0.95	-0.95	-0.94	-0.98	-0.98
cyclohexane	-0.92	-0.92	-0.96	-0.95	-0.97	-0.97

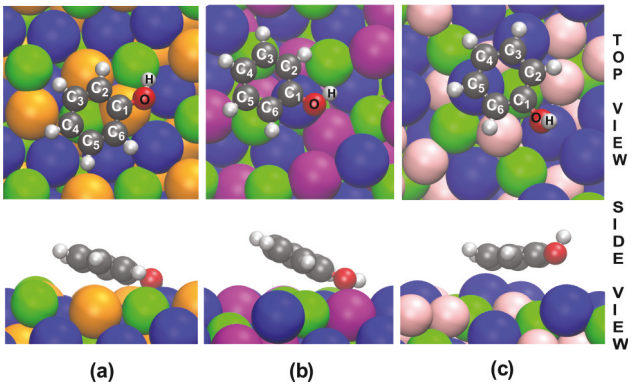

Fig. 3 Adsorption of phenol (C_6H_5OH) on (112) facet of (a) FeMoP (b) RuMoP, and (c) NiMoP catalyst. The orange, purple, pink, blue, and green colors represent Fe, Ru, Ni, Mo, and P atoms, respectively.

to note that both measurement methods were relative measurements based on a reference. The charge transfer in bimetallic phosphides have been shown to correlate well with electronegativity.[93] For example, Allred-Rochow electronegativity scale suggested the Ru is more electronegative compared to Mo, which would result in some electron donation to Ru causing Ru to be more negative. However, in Pauling electronegativity scale, Ru and Mo had almost equal electronegativity value. In this case, they both donated electrons to P almost equally causing both metals to be partially positive. In any case, Mo has a stronger influence towards the reaction pathway determination.

Table 3 Perpendicular distance (d, Å) of atoms and center of mass (COM) of phenol (C_6H_5OH), benzene (C_6H_6), cyclohexanol ($C_6H_{11}OH$), cyclohexene (C_6H_{10}), and cyclohexane (C_6H_{12}) from the surface after adsorption on (112) facet of FeMoP, RuMoP, and NiMoP catalyst by using optB88-vdW functional[a]

system	atom	C_6H_5OH	C_6H_6	$C_6H_{11}OH$	C_6H_{10}	C_6H_{12}
FeMoP	C_1	2.13	2.27	2.13	2.22	2.23
	C_2	2.35	2.37	2.35	2.38	2.38
	C_3	2.70	2.55	2.67	2.67	2.67
	C_4	2.84	2.62	2.83	2.73	2.75
	C_5	2.61	2.52	2.62	2.57	2.58
	C_6	2.27	2.34	2.27	2.27	2.29
	O	1.78	–	1.83	–	–
	H	1.61	–	1.65	–	–
	COM	2.48	2.44	2.48	2.51	2.50
RuMoP	C_1	2.27	2.21	2.28	2.33	2.33
	C_2	2.39	2.37	2.37	2.60	2.59
	C_3	2.97	2.81	2.75	2.78	2.76
	C_4	3.40	2.97	3.12	2.64	2.66
	C_5	3.27	2.23	2.01	2.44	2.46
	C_6	2.38	1.93	2.13	2.18	2.21
	O	1.81	–	1.77	–	–
	H	1.67	–	1.65	–	–
	COM	2.83	2.59	2.70	2.50	2.48
NiMoP	C_1	2.84	2.24	2.75	2.12	2.10
	C_2	2.80	2.34	2.78	2.35	2.35
	C_3	2.48	2.66	2.47	2.56	2.56
	C_4	2.45	2.86	2.45	2.56	2.57
	C_5	2.53	2.58	2.43	2.41	2.43
	C_6	2.58	2.34	2.33	2.17	2.17
	O	2.98	–	2.78	–	–
	H	3.88	–	3.73	–	–
	COM	2.25	2.23	2.18	2.31	2.33

[a] atom to atom distances between atoms of adsorbed phenol molecule and nearby surface atoms are given in Table S7.

3.2 Binding of selected species on the surface

The first step for the HDO reaction is the adsorption of phenol on (112) facet of FeMoP, RuMoP, and NiMoP catalysts. In order to find the most stable configuration (preferred binding mode) of phenol on the catalytic surface, we explored different molecule-surface bonding via the oxygen-lone pair and carbonic ring with Lewis acid sites and metal sites of the catalytic surface. We looked at both the horizontal and vertical orientation of phenol molecule with respect to the surface plane. We found that the adsorption energy is significantly higher for the horizontal orientation compared to the vertical orientation. In the horizontal configuration, apart from strong bonding of the phenolic oxygen with the surface, large interaction with the carbon-carbon π bonds and the surface metal sites occurs while only the oxygen atom interacts and creates a bond with the metal during phenol's vertical adsorption. In the optimized configuration, phenol is adsorbed in such a way that phenyl ring is tilted towards the surface with the oxygen pointing towards the surface for FeMoP and RuMoP catalyst whereas NiMoP catalyst surface shows that instead of adsorption due to the oxygen atom of phenol; adsorption through phenyl ring is preferred. The optimized stable configurations on (112) plane of FeMoP, RuMoP, and NiMoP catalyst, is provided in Fig. 3. These optimized structures are used as the initial structures for the HDO mechanisms studies. Furthermore, Fig. S2 illustrates adsorption of phenol on (111) facet of NiMoP, which is the most favorable surface for NiMoP, as mentioned earlier. Also, Fig. 3 and Fig. S2 demonstrate the most stable configuration of phenol that corresponds to the oxygen located atop on a Mo atom for all three kinds of catalytic systems. On (112) facet, phenol adsorption energies are -1.39, -1.29, and -1.21 eV for FeMoP, RuMoP, and NiMoP surface, respectively (see Table 2) by using optB88-vdW functional, all of these are in a similar range as with previous works investigating phenol adsorption on catalytic Pt,[94] Pd,[22,94] Rh,[20] Fe,[22] and Pd-Fe facets.[63] Additionally, Table S6 shows the comparison between adsorption energies of phenol on (112) and (111) facet of the NiMoP catalyst.

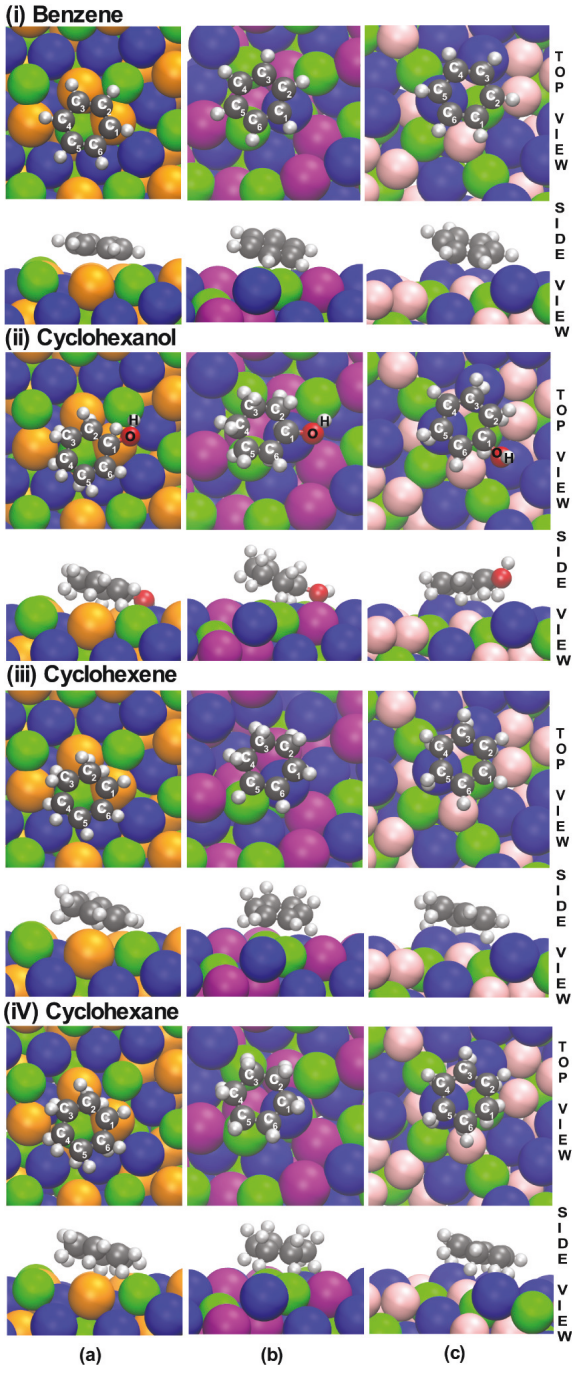

Fig. 4 Adsorption of (i) benzene (C_6H_6) (ii) cyclohexanol ($C_6H_{11}OH$), (iii) cyclohexene (C_6H_{10}), and (iv) cyclohexane (C_6H_{12}) on (112) facet of (a) FeMoP, (b) RuMoP, and (c) NiMoP catalyst. The orange, purple, pink, blue, and green colors represent Fe, Ru, Ni, Mo, and P atoms, respectively.

The adsorption energies are rationalized by calculating the distance of each atom of phenol from the surface. Table 3 reports that the oxygen to surface distance is 1.78, 1.81, and 2.98 Å whereas the phenolic hydrogen to surface distance is 1.61, 1.67, and 3.88 Å for FeMoP, RuMoP, and NiMoP system, respectively. The smaller distance between oxygen/hydrogen and surface suggests that adsorption of phenol through oxygen atom is preferable for the FeMoP and RuMoP system than the NiMoP system. Table 3 also shows that C_3, C_4, and C_5 carbon (for the atom numbering see Fig. 3) distances from the surface are smaller for NiMoP than FeMoP and RuMoP systems, which again support the fact that phenol adsorbed through phenyl ring rather than oxygen atom on the NiMoP surface. The average distance of phenyl ring is defined by the center of mass (COM) and it is 2.48, 2.83, and 2.25 Å for FeMoP, RuMoP, and NiMoP surface, respectively, which again confirms that on NiMoP surface phenol is adsorbed through the phenyl ring. The order for distances of oxygen/hydrogen to surface and COM to surface are FeMoP $<$ RuMoP $<$ NiMoP and NiMoP $<$ FeMoP $<$ RuMoP, respectively. The calculated atom distances in this study are in good agreement with previous results albeit with monometallic surfaces.[19,94,95] Furthermore, detailed atom to atom distances are given in Table S7.

Although we describe the HDO mechanisms in detail below, this section investigates the adsorption of different products (benzene, cyclohexanol, cyclohexene, and cyclohexane) of HDO reactions using optB88-vdW functional. We observed that a benzene molecule follows the same trend as phenol. As mentioned in Table 3, COM distance from the surface is 2.44, 2.59, and 2.23 Å for FeMoP, RuMoP, and NiMoP system, respectively for benzene. Although the order of COM distances from the surface is NiMoP $<$ FeMoP $<$ RuMoP but due to greater total partial charge on the FeMoP (+0.81 |e|) and RuMoP surface (+0.78 |e|) than NiMoP surface (+0.64 |e|) the adsorption energies are not in the same order. The adsorption energy for benzene is -1.73, -1.53, and -1.27 eV for FeMoP, RuMoP, and NiMoP surface, respectively, which indicates van der Waals (vdW) forces play an important role in adsorption. Interestingly, adsorption energy of cyclohexanol is -1.05, -1.13, and -1.17 eV for FeMoP, RuMoP, and NiMoP surface, respectively, and order for cyclohexanol energies is completely opposite of phenol due to more charge transfer between the oxygen of cyclohexanol and NiMoP surface. The adsorption energies of cyclohexene and cyclohexane are -0.97, -0.95, -0.98 eV, and -0.92, -0.96, -0.97 eV for FeMoP, RuMoP, and NiMoP surface, respectively, which indicate that there is not much adsorption energy difference between different catalytic surfaces for cyclohexene and cyclohexane. We have defined the atom name terminology in Fig. 4 for benzene, cyclohexanol, cyclohexene, and cyclohexane. Furthermore, the favorable adsorption site for H atom is on the top of Mo atom ($E_{AD} = \sim 0.18$ eV; see Table S8).

To compare results with van der Waals corrected optB88-vdW functional with non-corrected PW91 functional,[96–98] we evaluated the energetics associated with the binding of reactant (phenol) and products (benzene, cyclohexanol, cyclohexene, cyclohexane) on different catalytic surfaces with PW91 functional as well. As reported in Table 2, for all the adsorbed molecules the adsorption energies are higher for optB88-vdW functional as com-

pared to PW91 functional. The difference in adsorption energies is around 0.02 eV to 0.12 eV in magnitude for two different functionals. The strong or weak bonding of the molecules depends on the physisorption (van der Waals attraction) or covalently bonding nature of molecules on the catalytic surface. Partially filled d bands of transition metal contained catalysts provide great adsorption strength to aromatic rings. Due to the π electron cloud of phenol, benzene and cyclohexene ring, we observed higher adsorption energies on the catalytic surfaces as compared to the molecules without the π electron cloud like cyclohexanol and cyclohexane. Although the adsorption energies of cyclohexanol and cyclohexane are different for different catalytic surfaces, there is not much difference between different density functionals. We observe vdW corrections affect the activation energy barriers of different elementary steps involved in HDO reactions (see Table S9 for details). Fig. S3 displays a comparative study for FeMoP (112) facet surface with respect to two different functionals for direct deoxygenation (DDO) reaction. These differences in adsorption and activation energies and for these two functionals show that there is a significant effect of vdW interactions on these reactions. Therefore, we report all the results related to HDO mechanisms in the next sections, based on optB88-vdW functional in the current study.

3.3 Charge distribution upon adsorbate binding

The partial atomic charges of phenol in the gas and in the adsorbed state (shown in Table 4 and Table S10), illustrate that after adsorption there is a significant charge difference on phenolic oxygen and hydrogen (atoms of -OH group of phenol) upon adsorption on FeMoP and RuMoP catalytic systems but there is not much difference for NiMoP catalytic system. The partial charge of gas phase phenolic oxygen is -1.16 |e| which reduced by 0.13, 0.06, and 0.01 |e|, for FeMoP, RuMoP, and NiMoP catalytic surface, respectively. The partial atomic charge on the gas phase phenolic hydrogen is +0.66 |e| which changes by 0.15, 0.11, and 0.02 |e| for FeMoP, RuMoP, and NiMoP catalytic surface, respectively after adsorption.

The changes in the charge of phenolic oxygen and hydrogen after adsorption are significant for FeMoP and RuMoP catalytic system, but not for the NiMoP catalytic surface, which supports the fact that adsorption energy of phenol is more for FeMoP and RuMoP surface than NiMoP surface. Furthermore, change in charge of phenolic carbon (C_1 in Fig. 3) is more for NiMoP system ($\sim$ 0.36 |e| and $\sim$ 0.27 |e| for (112) and (111) plane, respectively) than FeMoP and RuMoP catalytic system ($\sim$ 0.05 |e| and $\sim$ 0.01 |e|, respectively) which supports the initial adsorption results that phenol adsorbed on NiMoP surface through phenyl ring rather than adsorbing through oxygen of phenol, can potentially lead to ring hydrogenation first. The atomic charges of other phenolic ring carbons (C_2 to C_6 in Fig. 3) in the gas phase and in the adsorbed state has been shown in Table 4.

Similarly, we evaluated the charge redistribution between the atoms of cyclohexanol and the catalytic surface, which is shown in Table 5. The charge on oxygen atom of cyclohexanol in the adsorbed state is -1.11, -1.00, and -0.97 |e|, and the charge on C_1 carbon atom is +0.40, +0.45, and +0.79 |e| for FeMoP, RuMoP, and NiMoP catalytic surface, respectively, whereas the charge of phenolic oxygen on the corresponding surfaces was -1.03, -1.10, and -1.15 |e| and the charge on phenolic C_1 was +0.44, +0.38, and +0.75 |e|, respectively. The order for the change in charge of oxygen and C_1 atoms is FeMoP $<$ RuMoP $<$ NiMoP. The maximum charge transfer between oxygen/C_1 and surface is observed for NiMoP surface which leads to large increase in C-O bond length.

Table 4 Partial atomic charge (q, |e|) on the individual atoms of phenol (C_6H_5OH) in the gas phase and on the(112) facet of FeMoP, RuMoP, and NiMoP catalysts

atom	gas phase	FeMoP	RuMoP	NiMoP
C_1	+0.39	+0.44	+0.38	+0.75
C_2	+0.06	– 0.06	+0.21	– 0.007
C_3	– 0.12	– 0.07	– 0.18	– 0.145
C_4	+0.002	– 0.08	+0.13	– 0.14
C_5	– 0.09	+0.06	– 0.22	– 0.26
C_6	– 0.12	– 0.07	+0.13	– 0.04
O	– 1.16	– 1.03	– 1.10	– 1.15
H	+0.66	+0.81	+0.77	+0.68

Table 5 Partial charge (q, |e|) on the individual atoms of cyclohexanol ($C_6H_{11}OH$) on the(112) facet of FeMoP, RuMoP, and NiMoP catalysts

atom	FeMoP	RuMoP	NiMoP
C_1	+0.40	+0.45	+0.79
C_2	– 0.02	+0.01	– 0.02
C_3	– 0.01	- -0.03	– 0.03
C_4	– 0.02	+0.09	– 0.05
C_5	+0.04	– 0.10	– 0.01
C_6	– 0.01	+0.07	– 0.01
O	– 1.11	– 1.00	– 0.97
H	+0.69	+0.73	+0.75

3.4 Direct deoxygenation reaction (DDO)

To understand the mechanistic aspects of deoxygenation reaction on different catalysts, we examined the activation energy barriers for elementary steps and the relative stability of the intermediate species. The first step in the DDO mechanism is the adsorption of phenol and hydrogen species in the form of $C_6H_5OH^*$ and H* (Equation (i) and (ii) in Scheme 1) as shown in Fig. 5 (a)-(b), Fig. S4 (a)-(b), and Fig. S5 (a)-(b) for FeMoP, RuMoP, and NiMoP catalyst, respectively. This leads to the formation of surface adsorbed phenyl group (C_6H_5*) and H_2O molecule (Equation (iii) in Scheme 1) due to the reaction between H* and hydroxyl group of $C_6H_5OH^*$, which is illustrated in Fig. 5 (c)-(d), Fig. S4 (c)-(d), and Fig. S5 (c)-(d).

In this elementary reaction step, the attack of surface-bound hydrogen atom on the phenolic oxygen leads to the transition state (TS1) (Fig. 5 (c), Fig. S4 (c), and Fig. S5 (c)), and E_A for this elementary step is 0.37, 0.48, and 0.8 eV for FeMoP, RuMoP, and NiMoP catalyst, respectively (see Fig. 6 and Table 6). Clearly, the FeMoP catalyst has lower E_A than RuMoP and NiMoP catalyst for this step. This result is supported by Bader charge analysis of the surface atoms of the catalysts which are shown in Table 1. As can be seen in Table 1, there is a greater total positive partial charge on the metallic species for FeMoP (i.e. +0.81 |e|) compared to the other two catalytic surfaces (i.e. +0.78, +0.64

$$C_6H_5OH(g) + * \leftrightarrow C_6H_5OH^* \quad \text{(i)}$$

$$H_2(g) + 2* \leftrightarrow 2H^* \quad \text{(ii)}$$

$$C_6H_5OH^* + H^* \leftrightarrow C_6H_5^* + H_2O^* \quad \text{(iii)}$$

$$C_6H_5^* \xleftrightarrow{\text{ring-rotation}} C_6H_5^* \quad \text{(iv)}$$

$$C_6H_5^* + H^* \leftrightarrow C_6H_6^* + * \quad \text{(v)}$$

$$H_2O^* \leftrightarrow H_2O(g) + * \quad \text{(vi)}$$

$$C_6H_6^* \leftrightarrow C_6H_6(g) + * \quad \text{(vii)}$$

Scheme 1 Elementary steps involved in DDO reaction pathway.

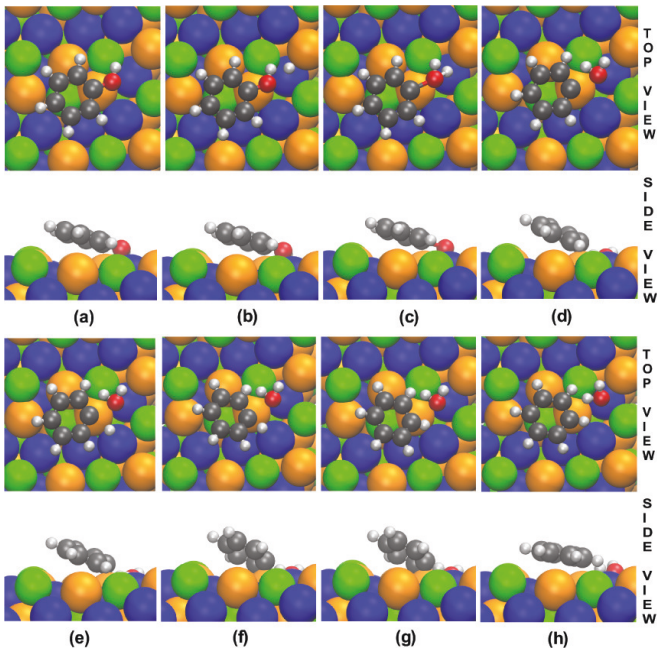

Fig. 5 Optimized structures of phenol (C_6H_5OH), benzene (C_6H_6), and reaction intermediates on the (112) facet of FeMoP during DDO reaction: (a) C_6H_5OH*, (b) C_6H_5OH* and H*, (c) C_6H_5-OH_2*(TS1), (d) C_6H_5* and OH_2*, (e) H*, C_6H_5*, and H_2O*, (f) H*, rotated C_6H_5*, and H_2O*, (g) C_6H_5-H* and H_2O*(TS3), and (h) C_6H_6* and H_2O*. The orange, blue, and green colors represent Fe, Mo, and P atoms, respectively.

|e| for RuMoP and NiMoP surface, respectively) which suggests FeMoP has more Lewis acidic character than the other two. After adsorption, C–O bond (gas phase bond length = 1.43 Å) of phenol is stretched significantly, as shown in Table 7. The increase in the bond length is 0.15, 0.10, and 0.02 Å for FeMoP, RuMoP, and NiMoP, respectively. However, for (111) facet of NiMoP the increase in C–O bond length is larger when compared to 112 facet (0.04 vs 0.02 Å). The order for bond length increase is FeMoP > RuMoP > NiMoP. The strong binding on the FeMoP surface leads to significant weakening of C–O bond and leads to lower E_A for C–O bond cleavage as well. We also observed (see Table 7) that there is not a significant change (0.02 Å or less) in O–H bond length after adsorption. This negligible change in O–H bond length after adsorption potentially precludes formation of phenoxy ion.

The next elementary step in this mechanism is the rotation of the phenyl ring (C_6H_5*) (see Fig. 5 (e)-(f), Fig. S4 (e)-(f), and Fig. S5 (e)-(f)) in the presence of surface adsorbed hydrogen species (H*) (Equation (iv) in Scheme 1). The E_A for this step is 0.15, 0.21, and 0.28 eV for FeMoP, RuMoP, and NiMoP catalytic surface, respectively, and the transition state for the same is labeled as TS2, which is shown in Fig. 6 and Table 6. E_A for the ring rotation step is again lowest for the FeMoP catalytic surface, which supports the next step (ring hydrogenation). The transition state for ring hydrogenation (C_6H_5-H*) is labeled as TS3. In this elementary step, the carbon atom of surface adsorbed rotated ring (C_6H_5*) forms bond with surface adsorbed hydrogen (H*), and leads to surface-adsorbed aromatic benzene ring C_6H_6 (Equation (v) in Scheme 1) as displayed in Fig. 5 (g)-(h), Fig. S4 (g)-(h), and Fig. S5 (g)-(h). The E_A for this step is 0.24, 0.28, and 0.89 eV for FeMoP, RuMoP, and NiMoP catalytic surface, respectively (Table 6). This demonstrates FeMoP surface is more active for the ring hydrogenation step in comparison to the other two catalytic systems. The binding energy of surface adsorbed C_6H_6* is -1.73, -1.53, and -1.27 eV for FeMoP, RuMoP, and NiMoP catalytic surface, respectively, which indicates a strong attraction of benzene to the FeMoP surface (see Table 2). Lastly, this adsorption step follows the desorption (Equation (vii) in Scheme 1) of benzene in form of C_6H_6 (g) with desorption energy of 1.53, 1.33, and 1.07 eV which proves it is an exothermic reaction. We also performed the same DDO reaction mechanism on (111) plane of NiMoP, and the E_A for TS1, TS2, and TS3 is 0.77, 0.28, and 0.88 eV which shows activation energy barriers for these three steps are little smaller than (112) plane but this change is not significant as shown in Table S11.

Overall, there are three key elementary steps associated with DDO pathway. Out of these three key elementary steps, the first step, which is the dissociation of phenolic C–O bond has the highest E_A for FeMoP and RuMoP catalytic surfaces. Interestingly, it is not the same case for the NiMoP catalytic surface where C–H

Table 6 Activation energy barriers (E_A, eV) of main elementary steps involved in DDO reaction pathway for phenol (C_6H_5OH) on (112) facet of FeMoP, RuMoP, and NiMoP catalysts

reaction step	FeMoP	RuMoP	NiMoP
C–O cleavage	0.37	0.48	0.8
ring rotation	0.15	0.21	0.28
C–H formation	0.24	0.28	0.89

Table 7 Bond length (r, Å) between two selected atoms of phenol (C_6H_5OH) and cyclohexanol ($C_6H_{11}OH$) after adsorption on (112) facet of FeMoP, RuMoP, and NiMoP catalyst by using optB88-vdW functional

system	molecule	bond	r
FeMoP	C_6H_5OH	C–O	1.58
		O–H	0.98
	$C_6H_{11}OH$	C–O	1.53
		O–H	0.97
RuMoP	C_6H_5OH	C–O	1.53
		O–H	0.98
	$C_6H_{11}OH$	C–O	1.57
		O–H	0.96
NiMoP	C_6H_5OH	C–O	1.45
		O–H	0.96
	$C_6H_{11}OH$	C–O	1.60
		O–H	0.96

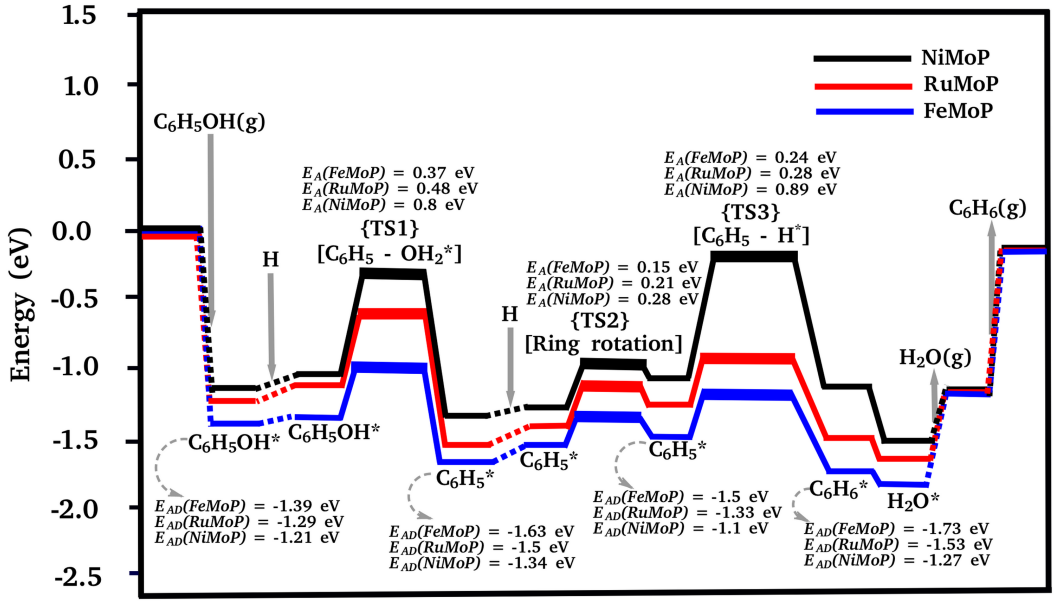

Fig. 6 Reaction energetics on the (112) facet during DDO reaction. The black, red, and blue colors represent NiMoP, RuMoP, and FeMoP catalyst, respectively.

$$C_6H_5OH(g) + * \leftrightarrow C_6H_5OH^* \quad \text{(i)}$$

$$4\,H_2(g) + 8* \leftrightarrow 8\,H^* \quad \text{(ii)}$$

$$C_6H_5OH^* + H^* \leftrightarrow C_6H_6{-}OH^* \quad \text{(iii)}$$

$$C_6H_6OH^* + 5\,H^* \leftrightarrow C_6H_{11}{-}OH^* \quad \text{(iv)}$$

$$C_6H_{11}OH^* + H^* \leftrightarrow C_6H_{11}^* + H_2O^* \quad \text{(v)}$$

$$C_6H_{11}^* + H^* \leftrightarrow C_6H_{12}^* \quad \text{(vi)}$$

$$H_2O^* \leftrightarrow H_2O(g) + * \quad \text{(vii)}$$

$$C_6H_{12}^* \leftrightarrow C_6H_{12}(g) + * \quad \text{(viii)}$$

Scheme 2 Elementary steps involved in RH-DO reaction pathway. (Equation (iv) shows five individual elementary hydrogenation steps)

bond formation step (ring hydrogenation step) is the rate-limiting step due to the highest E_A for both the facets considered.

3.5 Ring hydrogenation followed by deoxygenation (RH-DO) or dehydration (RH-DEHYD) reaction

There is a significant evidence that Ni and Mo-based bimetallic catalysts can promote ring hydrogenation. For example, Wang et al. showed that NiMoB bimetallic catalyst gives higher selectivity for cyclohexanol (∼74 mol%) and cyclohexane (∼20.6 mol%) than benzene (∼5.3 mol%).[56] Also recently published work by Bonita et al., demonstrates that RuMoP and NiMoP catalysts show greater selectivity for cyclohexane.[54] Thus, we examined the ring hydrogenation and deoxygenation/dehydration reaction (RH-DO/DEHYD) mechanisms (see Scheme 2 and 3), on (112) facet of FeMoP, RuMoP, and NiMoP catalysts as well as (111) facet of NiMoP.

The RH-DO reaction mechanism starts with the adsorption of phenol on the catalytic surface (Equation (i) in Scheme 2) as illustrated in Fig. 7 (a) for (112) facet of NiMoP. Fig. 7 (b)-(d) show the next step i.e. hydrogenation of ring where one double bond of the aromatic ring converts into a single bond and creates $C_6H_6OH^*$ in the presence of surface adsorbed H*(Equation (iii) in Scheme 2). The activation energy barrier for the first hydrogenation step is 1.1, 0.18, and 0.11 eV for (112) facet of FeMoP, RuMoP, and NiMoP, respectively. The hydrogenation step continues until the unsaturated aromatic ring converts into a saturated ring in the presence of surface adsorbed hydrogens (5H*) and forms surface adsorbed cyclohexanol ($C_6H_{11}OH^*$; Equation (iv) in Scheme 2) as shown in Fig. 7 (e). We have labeled transition states as TS1-6 for the hydrogenation steps, which are shown in Fig. S6. Table 8 shows that E_A values for hydrogenation steps are very high for FeMoP catalyst but are small for RuMoP and NiMoP catalytic surfaces which suggest RH-DO mechanism is not preferable for the FeMoP catalyst.

Table 8 shows that for the RuMoP and NiMoP catalysts, the activation energy barriers for ring hydrogenation steps are rather small (0.04 eV to 0.25 eV) with the lower E_A for NiMoP. Subsequently, in the presence of another surface adsorbed hydrogen (H*), dissociation of C–O bond occurs in the form of H_2O (Equa-

Table 8 Activation energy barriers (E_A, eV) of main elementary reaction steps involved in RH-DO/DEHYD reaction mechanism for phenol (C_6H_5OH) on (112) facet of FeMoP, RuMoP, and NiMoP catalysts with optB88-vdW functional

reaction step	FeMoP	RuMoP	NiMoP
C_1–H formation	1.1	0.18	0.11
C_2–H formation	0.92	0.25	0.12
C_3–H formation	0.84	0.11	0.04
C_4–H formation	0.80	0.14	0.08
C_5–H formation	0.83	0.09	0.12
C_6–H formation	0.70	0.05	0.07
C–O cleavage (RH-DO)	0.63	0.29	0.14
C–O cleavage (RH-DEHYD)	0.71	0.45	0.38

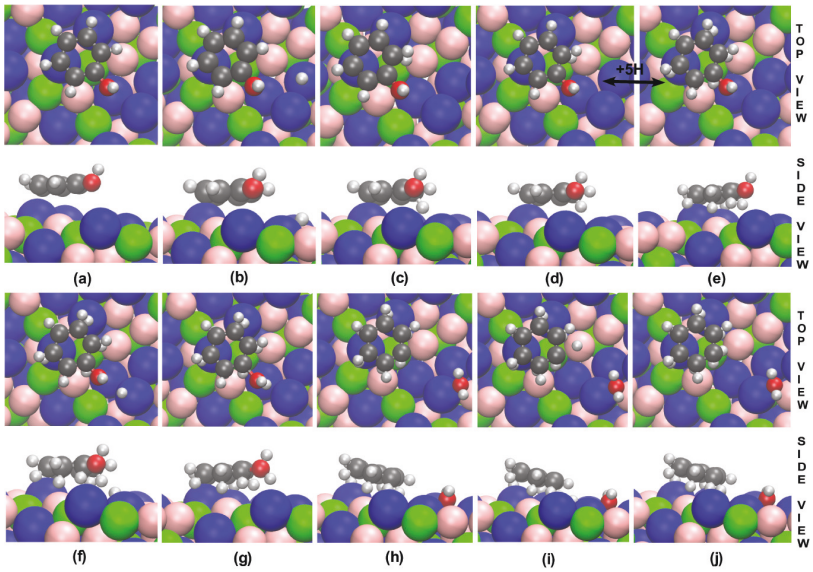

Fig. 7 Optimized structures of phenol (C_6H_5OH), cyclohexane (C_6H_{12}), and reaction intermediates on the (112) facet of NiMoP during RH-DO reaction: (a) C_6H_5OH*, (b) C_6H_5OH* and H*, (c) C_6H_5-HOH*(TS1), (d) C_6H_6OH*, (e) $C_6H_{11}OH$*, (f) $C_6H_{11}OH$* and H*, (g) C_6H_{11}-OH2* (TS7), (h) C_6H_{11}* and H_2O*, (i) C_6H_{11}*, H_2O* and H*, and (j) C_6H_{12}* and H_2O*. The pink, blue, and green colors represent Ni, Mo, and P atoms, respectively.

tion (v) in Scheme 2) which is illustrated in Fig. 7 (f)-(h). The activation energy barrier for the following step is 0.14 and 0.29 eV for NiMoP and RuMoP, respectively, which is very low in comparison of C–O bond scission E_A for the DDO pathway for the same two catalysts. Although the RH steps have similar E_A, the E_A for the final C–O bond cleavage step (Table 8), suggests that NiMoP is more selective for cyclohexane production due to the lower E_A (E_A (TS7) = 0.14 eV) than RuMoP (E_A (TS7) = 0.29 eV). Whereas, the E_A of C–O bond dissociation for FeMoP surface is 0.63 eV for the same reaction, which is very high in comparison of E_A of C–O bond dissociation (0.37 eV) in the DDO pathway. Upon examining the cyclohexanol bound on the surface, we find that C–O bond length is 1.53, 1.57, and 1.60 Å for FeMoP, RuMoP, and NiMoP, respectively (see Table 7), which supports low E_A values of C–O bond cleavage for NiMoP and RuMoP than FeMoP catalytic surface. As shown in the Fig. 7 (i)-(j), the last step for RH-DO reaction mechanism is cyclohexane (C_6H_{12}*) formation in the presence of another surface adsorbed hydrogen (H*) (Equation (vi) in Scheme 2) with activation energy E_A (TS8) = 0.17 eV for both RuMoP and NiMoP catalysts. We performed the same reaction mechanism on (111) facet of NiMoP and the results are shown in Table S12. We observed that E_A for C–O bond scission is approximately $\sim$ 0.02 eV smaller for (111) facet than (112) facet in this reaction.

It is also possible that cyclohexene formation is due to dehydration of cyclohexanol as it has been observed in previous experiments.[26,54] For this reason, we have examined the dehydration reaction pathway (RH-DEHYD) of cyclohexanol as shown in Fig. 8. The E_A for C–O cleavage step is 0.71, 0.45 eV, and 0.38 eV for FeMoP, RuMoP, and NiMoP, respectively. E_A results for this step show that this reaction is not feasible for FeMoP catalyst due to higher E_A than DDO reaction. On the other hand, activation

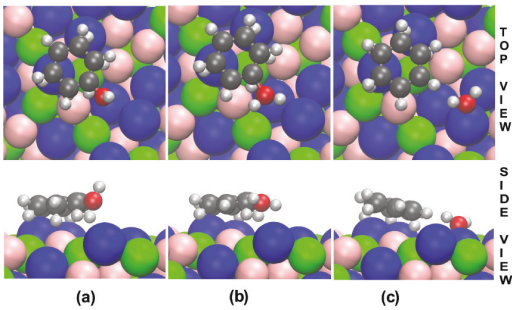

Fig. 8 Optimized structures of cyclohexanol ($C_6H_{11}OH$), cyclohexene (C_6H_{10}), and reaction intermediate on the (112) facet of NiMoP during RH-DEHYD reaction: (a) $C_6H_{11}OH$*, (b) C_6H_{11}-OH*(TS), and (c) C_6H_{10}* and H_2O*. The pink, blue, and green colors represent Ni, Mo, and P atoms, respectively.

energy barriers are smaller for this step during RH-DEHYD reaction for RuMoP and NiMoP catalytic surface than FeMoP catalyst, which shows there is a possibility for cyclohexene production on RuMoP and NiMoP surface. These activation energy barriers are smaller than DDO reaction pathway but higher than RH-DO reaction for NiMoP and RuMoP catalysts, which indicates the activity is less for cyclohexene production. The complete RH-DEHYD reaction mechanism is illustrated in Scheme 3.

Table 8 shows, for RH-DO and RH-DEHYD reactions, C–O bond cleavage step is the rate-limiting step due to the highest activation energy for NiMoP and RuMoP catalytic surfaces, whereas, the first ring hydrogenation step is the rate-limiting step for FeMoP.

3.6 Experimental validation of DFT results

We have conducted multiple experiments to find evidence supporting the favorable reaction pathways we proposed in sec-

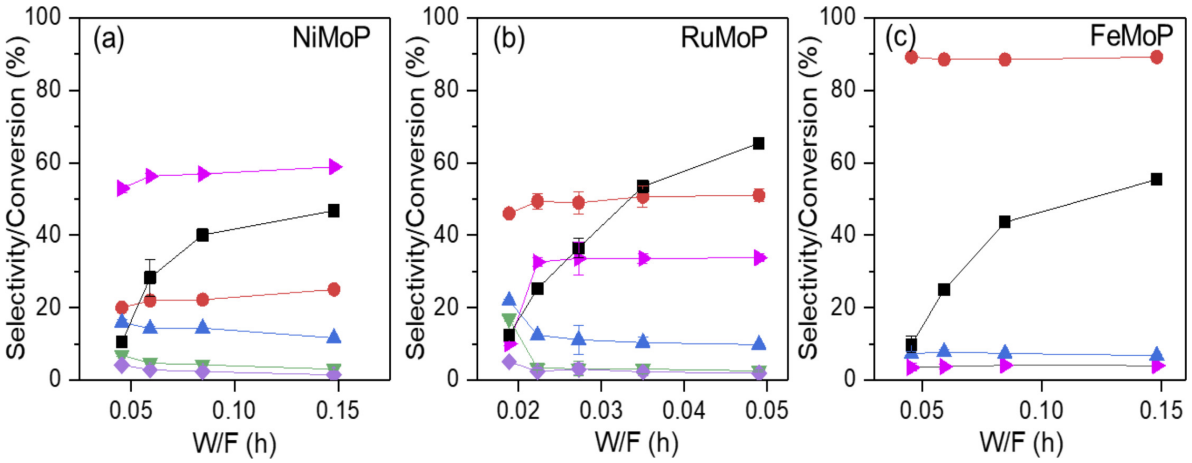

Fig. 9 Catalytic results of phenol HDO with (a) NiMoP, (b) RuMoP, and (c) FeMoP at 600 psig and 400 °C. The conversion is represented with black squares, while the product selectivity to benzene, cyclohexane, cyclohexene, cyclohexanol, and cyclohexanone is represented with the red circles, magenta sideway triangles, blue upward triangles, green downward triangles, and purple diamond, respectively.

$$C_6H_5OH(g) + * \leftrightarrow C_6H_5OH^* \quad \text{(i)}$$

$$3\,H_2(g) + 6* \leftrightarrow 6\,H^* \quad \text{(ii)}$$

$$C_6H_5OH^* + H^* \leftrightarrow C_6H_6{-}OH^* \quad \text{(iii)}$$

$$C_6H_6OH^* + 5\,H^* \leftrightarrow C_6H_{11}{-}OH^* \quad \text{(iv)}$$

$$C_6H_{11}OH^* \leftrightarrow C_6H_{10}^* + H_2O^* \quad \text{(v)}$$

$$H_2O^* \leftrightarrow H_2O(g) + * \quad \text{(vii)}$$

$$C_6H_{10}^* \leftrightarrow C_6H_{10}(g) + * \quad \text{(viii)}$$

Scheme 3 Elementary steps involved in RH-DEHYD reaction pathway. (Equation (iv) shows five individual elementary hydrogenation steps)

tion 3.4 and 3.5. The materials were tested for phenol HDO at 600 psig H_2 and 400 °C. The reaction results are plotted in Fig. 9 for NiMoP (Fig. 9 (a)), RuMoP (Fig. 9 (b)), and FeMoP (Fig. 9 (c)). The reaction results showed that the DDO selectivity was the highest with FeMoP resulting in close to 90 % in benzene production followed by RuMoP with 45 % benzene selectivity and NiMoP with only 20 % selectivity. The benzene selectivity was fairly constant for all conversions, which indicated that further benzene hydrogenation to cyclohexane was unlikely even at higher conversion for all catalysts.

The primary reaction product from phenol HDO using NiMoP was cyclohexane with 58 % selectivity at W/F of 0.15 h (Fig. 9 (a)). Ni-based phosphides such as Ni_2P have been reported as good ring hydrogenation catalysts even when Mo is present in the material for anisole hydrogenation to yield 80-95 % cyclohexane.[42] The high hydrogenation selectivity of NiMoP was also observed in our previous work at higher H_2 pressure of 750 psig, showing even further that NiMoP favors the hydrogenation pathway.[54] Similarly, phenol hydrogenation to cyclohexane was also observed with RuMoP (33 % selectivity, Fig. 9 (b)), yet higher amounts of benzene were collected (∼ 50 %). Interestingly, with RuMoP, the cyclohexane selectivity was only 10 % at low W/F but increases at higher W/F due to subsequent cascade reactions involving cyclohexanone, cyclohexanol, and cyclohexane. This can be observed in the decreasing selectivity of cyclohexene and cyclohexanol, while the selectivity to benzene remained nearly invariant. In comparison, cyclohexanol and cyclohexanone were observed in trace amounts during phenol HDO with FeMoP (Fig. 9 (c)), which we have observed in previous studies at different pressures at 750 psig. The benzene selectivity was unchanged with the two pressures because both H_2 pressures (600 psig and 750 psig) provide excess H_2 to the reaction system.

The experimental results agreed with the predicted pathway from the DFT calculations. Since the DDO pathway is the most favorable for FeMoP, selectivity to benzene was expected to be dominant. Additionally, the calculated bond distance between oxygen and surface was the shortest in FeMoP causing a stronger surface to oxygen bond, and thus more favorable to direct C-O bond cleavage. Inversely, NiMoP catalyst exhibited the highest hydrogenation selectivity because RH-DO/DEHYD pathway is energetically favored.

As observed in the experiments, although overall conversion of phenol is higher for RuMoP at low W/F (∼ 0.05 h) than FeMoP and NiMoP, the phenol selectivity to benzene is the highest for FeMoP and lowest for NiMoP. In contrast, phenol selectivity to cyclohexane is the highest for NiMoP and lowest for FeMoP. These results match with activation energies obtained through DFT for C–O bond cleavage which show that E_A order for DDO pathway is FeMoP (0.37 eV) > RuMoP (0.48 eV) > NiMoP (0. 8 eV) whereas order for RH-DO/DEHYD pathway is NiMoP (0.14/0.38 eV) > RuMoP (0.29/0.45 eV) > FeMoP (0.63/0.71 eV). The phenol orientation (parallel or tilted) influences the E_A which depends on surface Lewis acidity or oxophilicity as reported in the past research.[36,99–101] Our observations are consistent with previous works that show carbon and oxygen binding energies on transition metal surfaces can be good descriptors for the turnover frequencies.[36,99,102–107] Our calculations support the experimental findings that RuMoP is the most active catalytic surface that favors both DDO and RH-DO/DEHYD pathways for phenol conversion. However, in future, microkinetic model based approach

will be utilized to understand the catalytic activity and selectivity trends observed in the present study.

4 Conclusions

We have examined the mechanism of hydrodeoxygenation of phenol on three different bimetallic phosphides MMoP (M=Fe, Ru, and Ni). Based on the DFT calculations, phenol HDO through DDO pathway was the most favorable for the FeMoP catalyst leading to the benzene formation. On the opposite side, phenol HDO in NiMoP and RuMoP catalysts would most likely occur through RH-DO or RH-DEHYD pathway to produce cyclohexene and/or cyclohexane. These results are in good agreement with the product distribution observed from the experiments performed in a flow reactor at 600 psig and 400 °C. Partial charges on the surface atoms showed that there was a synergistic effect between both metal and phosphorus atoms in bimetallic phosphides that was responsible for C–O bond scission of phenol due to the formation of Lewis acid sites on the surface. Furthermore, elongation of C–O bond length upon adsorption was a good descriptor for the activation energy barrier for the C–O bond scission.

Conflicts of interest

There are no conflicts to declare.

Acknowledgements

The computational work was partially supported by NSF CAREER grant (CBET-1752036). The experimental part of this work was funded through NSF CAREER (CBET-1351609), Sustainable Energy Initiative at University of Notre Dame, Center for Environmental Science and Technology at Notre Dame, and Advanced Photon Source (DE-AC02- 06CH11357). This research used resources at the High Performance Computing Collaboratory at Mississippi State University. This research also used resources of the National Energy Research Scientific Computing Center, a DOE Office of Science User Facility supported by the Office of Science of the U.S. Department of Energy under Contract No. DE-AC02-05CH11231. We acknowledge VESTA, CANVAS, and VMD for use of their software to create images of the crystal structures contained in this manuscript. We also would like to thank the Material Characterization Facility at the University of Notre Dame.

Notes and references

1 J. Popp, Z. Lakner, M. Harangi-Rakos and M. Fari, *Renew. & Sust. Energ. Rev.*, 2014, **32**, 559–578.

2 O. Edenhofer, R. Pichs-Madruga, Y. Sokona, K. Seyboth, P. Matschoss, S. Kadner, T. Zwickel, P. Eickemeier, G. Hansen, S. Schlömer and C. von Stechow, *Prepared By Working Group III of the Intergovernmental Panel on Climate Change, Cambridge University Press, Cambridge, UK.*, 2011.

3 M. Verma, S. Godbout, S. Brar, O. Solomatnikova, S. Lemay and J. Larouche, *Int. J. Chem. Eng.*, 2012, **2012**, 542426.

4 J. Zakzeski, P. C. Bruijnincx, A. L. Jongerius and B. M. Weckhuysen, *Chem. Rev.*, 2010, **110**, 3552–3599.

5 J. J. Bozell and G. R. Petersen, *Green Chem.*, 2010, **12**, 539–554.

6 A. Lappas, M. Samolada, D. Iatridis, S. Voutetakis and I. Vasalos, *Fuel*, 2002, **81**, 2087–2095.

7 D. Mohan, C. U. Pittman and P. H. Steele, *Energy & fuels*, 2006, **20**, 848–889.

8 H. Wang, J. Male and Y. Wang, *Energy & fuels*, 2013, **3**, 1047–1070.

9 T. Dickerson and J. Soria, *Energies*, 2013, **6**, 514–538.

10 G. W. Huber, S. Iborra and A. Corma, *Chem. Rev.*, 2006, **106**, 4044–4098.

11 R. D. Perlack, L. M. Eaton, A. F. Turhollow Jr, M. H. Langholtz, C. C. Brandt, M. E. Downing, R. L. Graham, L. L. Wright, J. M. Kavkewitz, A. M. Shamey and R. G. Nelson, 2011.

12 C. Liu, H. Wang, A. M. Karim, J. Sun and Y. Wang, *Chem. Soc. Rev.*, 2014, **43**, 7594–7623.

13 R. L. McCormick, M. A. Ratcliff, E. Christensen, L. Fouts, J. Luecke, G. M. Chupka, J. Yanowitz, M. Tian and M. Boot, *Energy & Fuels*, 2015, **29**, 2453–2461.

14 V. Balan, *ISRN biotechnology*, 2014, **2014**, 463074.

15 M. I. Jahirul, M. G. Rasul, A. A. Chowdhury and N. Ashwath, *Energies*, 2012, **5**, 4952–5001.

16 M. Badawi, J.-F. Paul, S. Cristol and E. Payen, *Catal. Commun.*, 2011, **12**, 901–905.

17 L. Nie, P. M. de Souza, F. B. Noronha, W. An, T. Sooknoi and D. E. Resasco, *J. Mol. Catal. A: Chem.*, 2014, **388**, 47–55.

18 F. Massoth, P. Politzer, M. Concha, J. Murray, J. Jakowski and J. Simons, *J. Phys. Chem. B*, 2006, **110**, 14283–14291.

19 Y. Yoon, R. Rousseau, R. S. Weber, D. Mei and J. A. Lercher, *J. Am. Chem. Soc.*, 2014, **136**, 10287–10298.

20 D. Garcia-Pintos, J. Voss, A. D. Jensen and F. Studt, *J. Phys. Chem. C*, 2016, **120**, 18529–18537.

21 H. Liu, T. Jiang, B. Han, S. Liang and Y. Zhou, *Science*, 2009, **326**, 1250–1252.

22 A. J. Hensley, Y. Wang and J.-S. McEwen, *ACS Catal.*, 2014, **5**, 523–536.

23 R. C. Nelson, B. Baek, P. Ruiz, B. Goundie, A. Brooks, M. C. Wheeler, B. G. Frederick, L. C. Grabow and R. N. Austin, *ACS Catal.*, 2015, **5**, 6509–6523.

24 M. Rubeš, J. He, P. Nachtigall and O. Bludskỳ, *J. Mol. Catal. A: Chem.*, 2016, **423**, 300–307.

25 J. Zhong, J. Chen and L. Chen, *Catal. Sci. Technol.*, 2014, **4**, 3555–3569.

26 W. Song, Y. Liu, E. Baráth, C. Zhao and J. A. Lercher, *Green Chem.*, 2015, **17**, 1204–1218.

27 E. Furimsky, *Appl. Catal., A: General*, 2000, **199**, 147–190.

28 C. Zhao, Y. Kou, A. A. Lemonidou, X. Li and J. A. Lercher, *Angew. Chem.*, 2009, **121**, 4047–4050.

29 J. Tavizón-Pozos, V. Suárez-Toriello, P. del Ángel and J. de los Reyes, *Int. J. Chem. Reactor Eng.*, 2016, **14**, 1211–1223.

30 Y.-C. Lin, C.-L. Li, H.-P. Wan, H.-T. Lee and C.-F. Liu, *Energy & Fuels*, 2011, **25**, 890–896.

31 W. Zhang, J. Chen, R. Liu, S. Wang, L. Chen and K. Li, *ACS Sustain. Chem. Eng.*, 2014, **2**, 683–691.

32 H. Shafaghat, P. S. Rezaei and W. M. A. W. Daud, *RSC Adv.*, 2015, **5**, 33990–33998.

33 Z. Si, X. Zhang, C. Wang, L. Ma and R. Dong, *Catalysts*, 2017, **7**, 169.

34 I. Gandarias and P. L. Arias, *Hydrotreating catalytic processes for oxygen removal in the upgrading of bio-oils and biochemicals*, InTech, 2013.

35 Q. Tan, G. Wang, L. Nie, A. Dinse, C. Buda, J. Shabaker and D. E. Resasco, *ACS Catal.*, 2015, **5**, 6271–6283.

36 A. Robinson, G. A. Ferguson, J. R. Gallagher, S. Cheah, G. T. Beckham, J. A. Schaidle, J. E. Hensley and J. W. Medlin, *ACS Catal.*, 2016, **6**, 4356–4368.

37 P. M. de Souza, R. C. Rabelo-Neto, L. E. Borges, G. Jacobs, B. H. Davis, D. E. Resasco and F. B. Noronha, *ACS Catal.*, 2017, **7**, 2058–2073.

38 A. J. Hensley, Y. Wang, D. Mei and J. McEwen, *ACS Catal.*, 2018, **8**, 2200–2208.

39 W.-S. Lee, Z. Wang, R. J. Wu and A. Bhan, *J. Catal.*, 2014, **319**, 44–53.

40 B. Dhandapani, T. St Clair and S. Oyama, *Appl. Catal., A*, 1998, **168**, 219–228.

41 S. Boullosa-Eiras, R. Lødeng, H. Bergem, M. Stöcker, L. Hannevold and E. A. Blekkan, *Catal. Today*, 2014, **223**, 44–53.

42 K. Li, R. Wang and J. Chen, *Energy & Fuels*, 2011, **25**, 854–863.

43 V. Whiffen and K. Smith, *Top. Catal.*, 2012, **55**, 981–990.

44 S.-K. Wu, P.-C. Lai, Y.-C. Lin, H.-P. Wan, H.-T. Lee and Y.-H. Chang, *ACS Sustainable Chem. Eng.*, 2013, **1**, 349–358.

45 H. Zhao, D. Li, P. Bui and S. Oyama, *Appl. Catal., A: General*, 2011, **391**, 305–310.

46 J. Cecilia, A. Infantes-Molina, E. Rodríguez-Castellón, A. Jiménez-López and S. Oyama, *Appl. Catal., B: Environmental*, 2013, **136**, 140–149.

47 P. Bui, J. A. Cecilia, S. T. Oyama, A. Takagaki, A. Infantes-Molina, H. Zhao, D. Li, E. Rodríguez-Castellón and A. J. López, *J. Catal.*, 2012, **294**, 184–198.

48 R. H. Bowker, M. C. Smith, M. L. Pease, K. M. Slenkamp, L. Kovarik and M. E. Bussell, *ACS Catal.*, 2011, **1**, 917–922.

49 Y. He and S. Laursen, *ACS Catal.*, 2017, **7**, 3169–3180.

50 J.-S. Moon and Y.-K. Lee, *Top. Catal.*, 2015, **58**, 211–218.

51 D. J. Rensel, S. Rouvimov, M. E. Gin and J. C. Hicks, *J. Catal.*, 2013, **305**, 256–263.

52 D. J. Rensel, J. Kim, Y. Bonita and J. C. Hicks, *Appl. Catal., A: General*, 2016, **524**, 85–93.

53 D. J. Rensel, J. Kim, V. Jain, Y. Bonita, N. Rai and J. C. Hicks, *Catal. Sci. Technol.*, 2017, **7**, 1857–1867.

54 Y. Bonita and J. C. Hicks, *J. Phys. Chem. C*, 2018, **122**, 13322–13332.

55 W. Wang, Y. Yang, H. Luo, H. Peng and F. Wang, *Ind. Eng. Chem. Res.*, 2011, **50**, 10936–10942.

56 W. Wang, Y. Yang, J. Bao and H. Luo, *Catal. Commun.*, 2009, **11**, 100–105.

57 M. Shetty, K. Murugappan, T. Prasomsri, W. H. Green and Y. Roman-Leshkov, *J. Catal.*, 2015, **331**, 86–97.

58 M. Saidi, F. Samimi, D. Karimipourfard, T. Nimmanwudipong, B. C. Gates and M. R. Rahimpour, *Energy & Environmental Science*, 2014, **7**, 103–129.

59 Z. Yu, Y. Wang, Z. Sun, X. Li, A. Wang, D. Camaioni and J. A. Lercher, *Green Chem.*, 2018, **20**, 609–619.

60 D. Kubička and L. Kaluža, *Appl. Catal., A: General*, 2010, **372**, 199–208.

61 J. Chen, Y. Yang, H. Shi, M. Li, Y. Chu, Z. Pan and X. Yu, *Fuel*, 2014, **129**, 1–10.

62 A. M. Robinson, J. E. Hensley and J. W. Medlin, *ACS Catal.*, 2016, **6**, 5026–5043.

63 J. Sun, A. M. Karim, H. Zhang, L. Kovarik, X. S. Li, A. J. Hensley, J.-S. McEwen and Y. Wang, *J. Catal.*, 2013, **306**, 47–57.

64 W. Yu, K. Xiong, N. Ji, M. D. Porosoff and J. G. Chen, *J. Catal.*, 2014, **317**, 253–262.

65 R. G. Parr, *Horizons of Quantum Chemistry*, 1980, 5–15.

66 A. D. Becke, *J. Chem. Phys.*, 2014, **140**, 18A301.

67 G. Kresse and J. Hafner, *Phys. Rev. B*, 1993, **47**, 558–561.

68 G. Kresse and J. Furthmüller, *Comput. Mater. Sci.*, 1996, **6**, 15–50.

69 G. Kresse and J. Hafner, *Phys. Rev. B*, 1994, **49**, 14251–14269.

70 G. Kresse and J. Hafner, *Phys. Rev. B*, 1996, **54**, 11169–11186.

71 J. Klimeš, D. R. Bowler and A. Michaelides, *Phys. Rev. B*, 2011, **83**, 195131.

72 J. Klimeš, D. R. Bowler and A. Michaelides, *J. Phys. Condens. Matter*, 2009, **22**, 022201.

73 P. E. Blöchl, *Phy. Rev. B*, 1994, **50**, 17953–17979.

74 G. Kresse and D. Joubert, *Phy. Rev. B*, 1999, **59**, 1758–1775.

75 P. Stephens, F. Devlin, C. Chabalowski and M. J. Frisch, *J. Phys. Chem.*, 1994, **98**, 11623–11627.

76 M. Methfessel and A. Paxton, *Phy. Rev. B*, 1989, **40**, 3616–3621.

77 A. Genova and M. Pavanello, *J. Phys. Condens. Matter*, 2015, **27**, 495501.

78 W. Tang, E. Sanville and G. Henkelman, *Phy. Rev. B*, 2009, **21**, 084204.

79 E. Sanville, S. D. Kenny, R. Smith and G. Henkelman, *J. Comp. Phys.*, 2007, **28**, 899–908.

80 G. Henkelman, A. Arnaldsson and H. Jónsson, *Comput. Mater. Sci.*, 2006, **36**, 354–360.

81 M. Yu and D. R. Trinkle, *J. Chem. Phys.*, 2011, **134**, 064111.

82 G. Henkelman and H. Jónsson, *J. Chem. Phys.*, 2000, **113**, 9978–9985.

83 G. Henkelman and H. Jónsson, *J. Chem. Phys.*, 1999, **111**, 7010–7022.

84 H. Jónsson, G. Mills and K. W. Jacobsen, *Classical and quantum dynamics in condensed phase simulations*, 1998, 385–404.

85 G. Henkelman and H. Jónsson, *J. Chem. Phys.*, 2000, **113**, 9901–9904.

86 P. E. Blanchard, A. P. Grosvenor, R. G. Cavell and A. Mar, *Chem. Mater.*, 2008, **20**, 7081–7088.
87 P. E. Blanchard, A. P. Grosvenor, R. G. Cavell and A. Mar, *J. Mater. Chem.*, 2009, **19**, 6015–6022.
88 A. P. Grosvenor, R. G. Cavell and A. Mar, *J. Solid State Chem.*, 2008, **181**, 2549–2558.
89 A. P. Grosvenor, R. G. Cavell and A. Mar, *Controlled Assembly and Modification of Inorganic Systems*, 2009, **133**, 41–92.
90 C. I. Hiley, M. R. Lees, J. M. Fisher, D. Thompsett, S. Agrestini, R. I. Smith and R. I. Walton, *Angew Chen Int Edit*, 2014, **53**, 4423–4427.
91 S. Trudel, E. D. Crozier, R. A. Gordon, P. S. Budnik and R. H. Hill, *J. Solid State Chem.*, 2011, **184**, 1025–1035.
92 A. M. Beale, M. Paul, G. Sankar, R. J. Oldman, C. R. A. Catlow, S. French and M. Fowles, *J. Mater. Chem.*, 2009, **19**, 4391–4400.
93 A. P. Grosvenor, R. G. Cavell and A. Mar, *J. Solid State Chem.*, 2007, **180**, 2702–2712.
94 G. Li, J. Han, H. Wang, X. Zhu and Q. Ge, *ACS Catal.*, 2015, **5**, 2009–2016.
95 M. L. Honkela, J. Björk and M. Persson, *Phys. Chem. Chem. Phys.*, 2012, **14**, 5849–5854.
96 J. P. Perdew, J. A. Chevary, S. H. Vosko, K. A. Jackson, M. R. Pederson, D. J. Singh and C. Fiolhais, *Phys. Rev. B*, 1992, **46**, 6671–6687.
97 J. P. Perdew and Y. Wang, *Phys. Rev. B*, 1992, **46**, 12947–12954.
98 J. P. Perdew, J. Chevary, S. Vosko, K. A. Jackson, M. R. Pederson, D. Singh and C. Fiolhais, *Phys. Rev. B*, 1993, **48**, 4978.
99 F. Yang, D. Liu, Y. Zhao, H. Wang, J. Han, Q. Ge and X. Zhu, *ACS Catal.*, 2018, **8**, 1672–1682.
100 Q. Tan, G. Wang, A. Long, A. Dinse, C. Buda, J. Shabaker and D. E. Resasco, *J. Catal.*, 2017, **347**, 102–115.
101 P. M. de Souza, L. Nie, L. E. Borges, F. B. Noronha and D. E. Resasco, *Catalysis letters*, 2014, **144**, 2005–2011.
102 F. Jalid, T. S. Khan, F. Q. Mir and M. A. Haider, *J. Catal.*, 2017, **353**, 265–273.
103 A. C. Lausche, H. Falsig, A. D. Jensen and F. Studt, *Catal. Lett.*, 2014, **144**, 1968–1972.
104 H. Mayr and A. R. Ofial, *Angew. Chem. Int. Ed.*, 2006, **45**, 1844–1854.
105 P. Mäki-Arvela and D. Y. Murzin, *Catalysts*, 2017, **7**, 265.
106 Y. Hong, H. Zhang, J. Sun, K. M. Ayman, A. J. Hensley, M. Gu, M. H. Engelhard, J.-S. McEwen and Y. Wang, *ACS Catal.*, 2014, **4**, 3335–3345.
107 B. Seemala, C. M. Cai, R. Kumar, C. E. Wyman and P. Christopher, *ACS Sustain. Chem. Eng.*, 2018, **6**, 2152–2161.

Mechanistic Insights into Hydrodeoxygenation of Phenol on Bimetallic Phosphide Catalysts

Varsha Jain,[a] Yolanda Bonita,[b] Alicia Brown,[a‡] Anna Taconi,[a‡] Jason C. Hicks,[b] and Neeraj Rai[a*]

[a] *Dave C. Swalm School of Chemical Engineering and Center for Advanced Vehicular Systems, Mississippi State University, Mississippi State, Mississippi 39762, United States.*

[b] *Department of Chemical and Biomolecular Engineering, 182 Fitzpatrick Hall, University of Notre Dame, Indiana 46556, United States.*

‡ *Authors AB and AT contributed equally.*

E-mail: neerajrai@che.msstate.edu

Phone: (+1) 662-325-0790. Fax: (+1) 662-325-2482

X-ray diffraction (XRD) patterns

The crystal structures of the materials were confirmed using powder XRD in Figure 1. The XRD patterns of RuMoP, NiMoP, and FeMoP are plotted in Figure S1 (a), S1 (c), and S1(e) respectively with their corresponding reference pattern in Figure S1 (b), S1 (d), and S1 (f). The three most dominant peaks are marked with stars for the orthorhombic RuMoP and FeMoP, while the three most dominant peaks in NiMoP are marked with dots. The most dominant peak in FeMoP and RuMoP observed in XRD are (112) peak, while (111) facet is the most dominant in NiMoP samples. The XRD results confirmed that the materials are solid solution of bimetallic phosphides and are not mixtures.

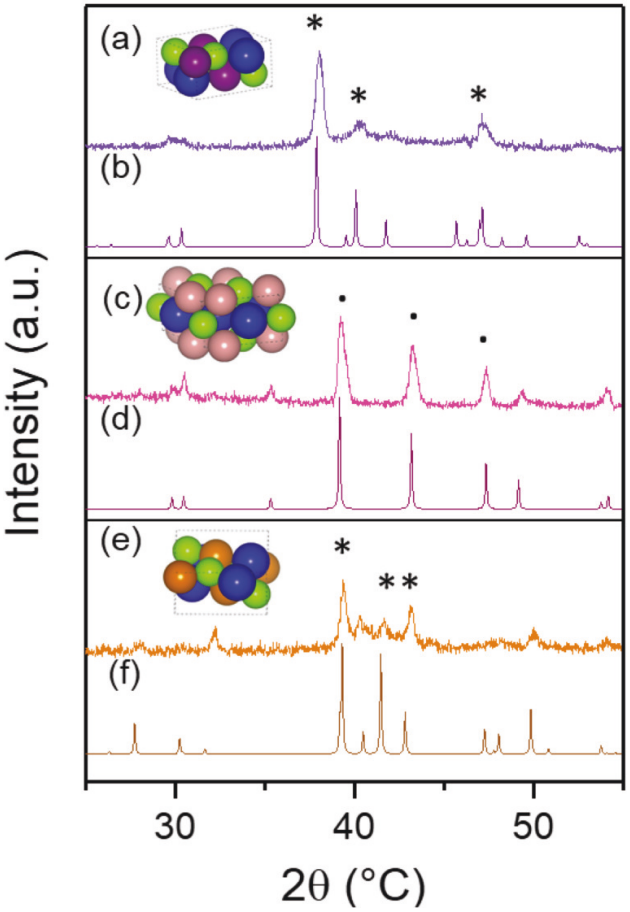

Figure S1: XRD pattern of (a) RuMoP (b) RuMoP reference pattern (PDF 04-015-7732) (c) NiMoP (d) NiMoP reference pattern (PDF 00-031-0873), (e) FeMoP (f) FeMoP reference pattern (PDF 04-001-4637).

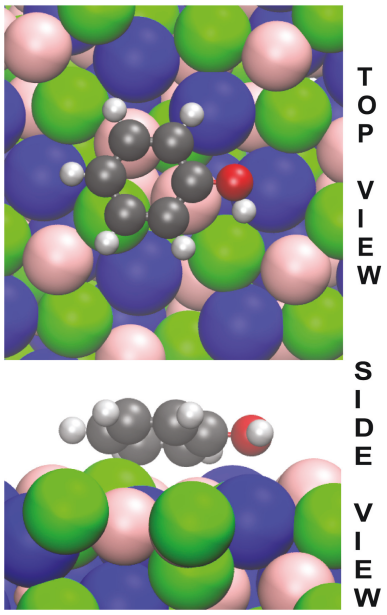

Figure S2: Adsorption of phenol (C_6H_5OH) on (111) facet of NiMoP catalyst.

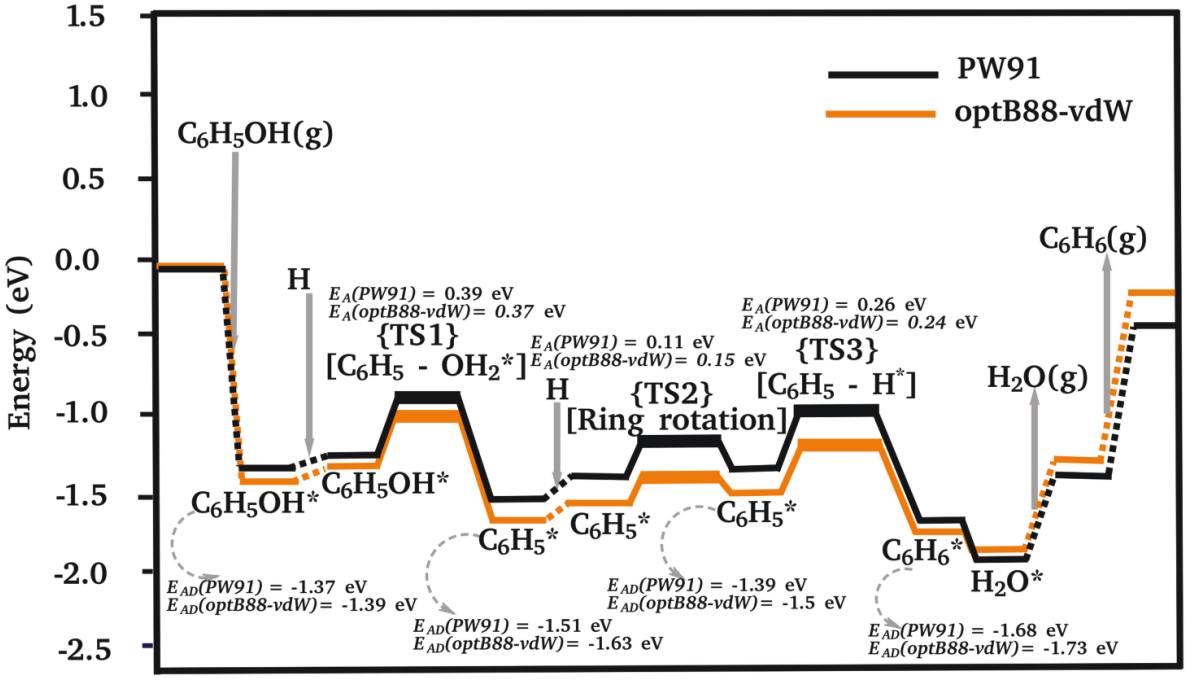

Figure S3: Reaction energetics on the (112) facet of FeMoP catalyst during DDO reaction. The black and orange colors represent results for PW91 and optB88-vdW functionals.

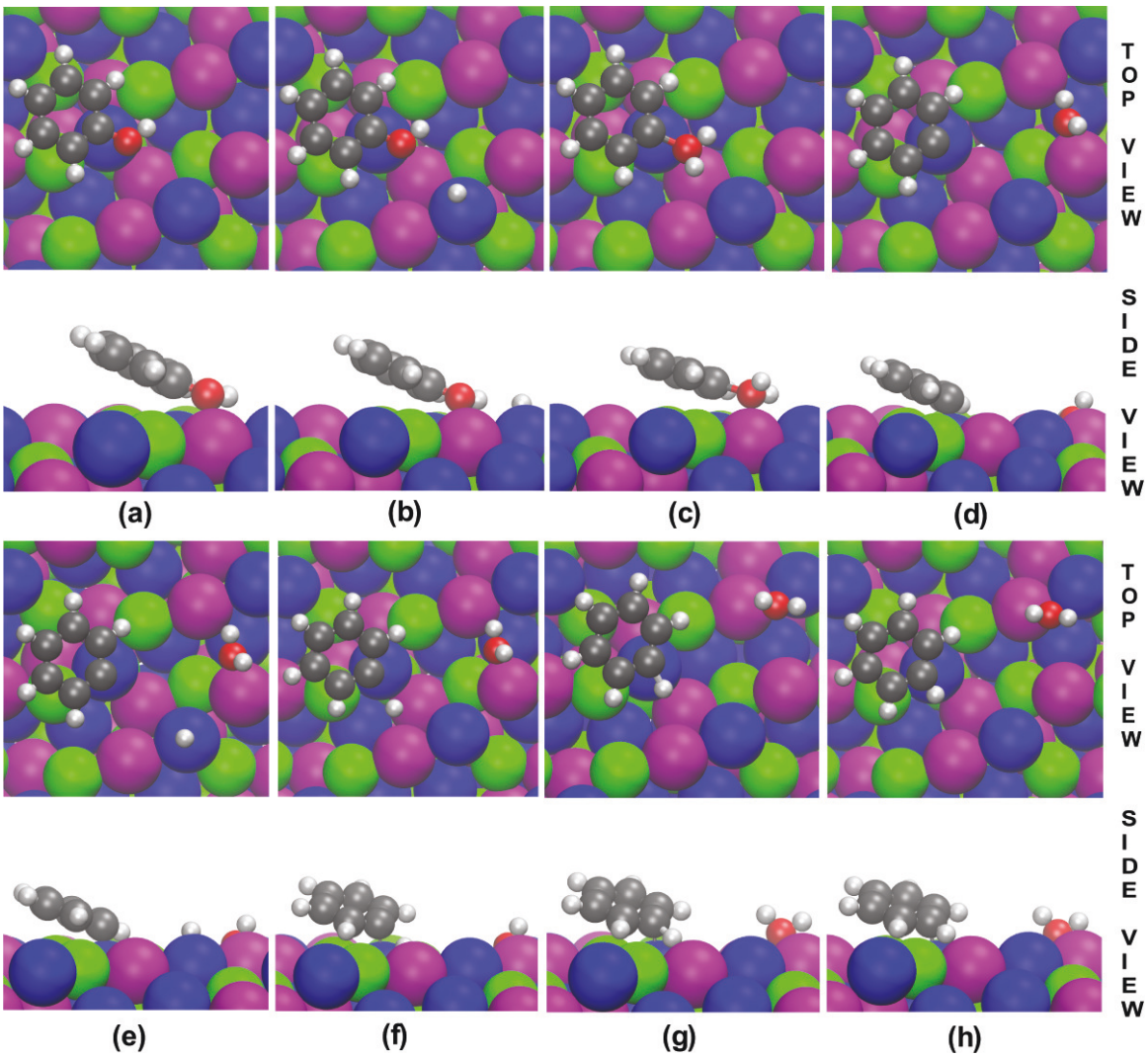

Figure S4: Optimized structures of phenol (C_6H_5OH), benzene (C_6H_6), and reaction intermediates on the (112) facet of RuMoP during DDO reaction: (a) C_6H_5OH*, (b) C_6H_5OH* and H*, (c) C_6H_5-OH_2*(TS1), (d) C_6H_5* and OH_2*, (e) H*, C_6H_5*, and H_2O*, (f) H*, rotated C_6H_5*, and H_2O*, (g) C_6H_5-H* and H_2O*(TS3), and (h) C_6H_6* and H_2O*. The purple, blue, and green colors represent Ru, Mo, and P atoms, respectively.

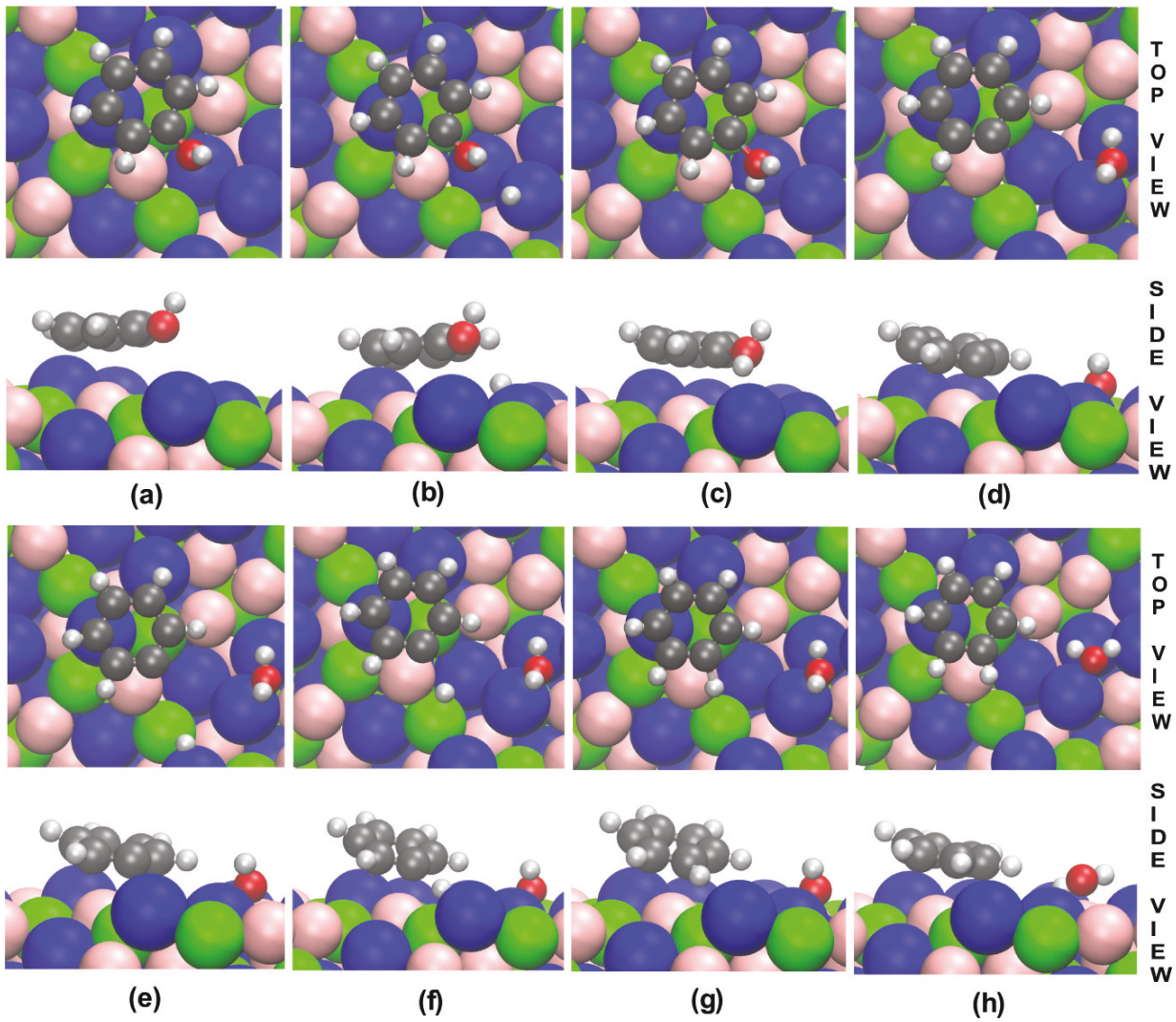

Figure S5: Optimized structures of phenol (C_6H_5OH), benzene (C_6H_6), and reaction intermediates on the (112) facet of NiMoP during DDO reaction: (a) C_6H_5OH*, (b) C_6H_5OH* and H*, (c) C_6H_5-OH_2*(TS1), (d) C_6H_5* and OH_2*, (e) H*, C_6H_5*, and H_2O*, (f) H*, rotated C_6H_5*, and H_2O*, (g) C_6H_5-H* and H_2O*(TS3), and (h) C_6H_6* and H_2O*. The pink, blue, and green colors represent Ni, Mo, and P atoms, respectively.

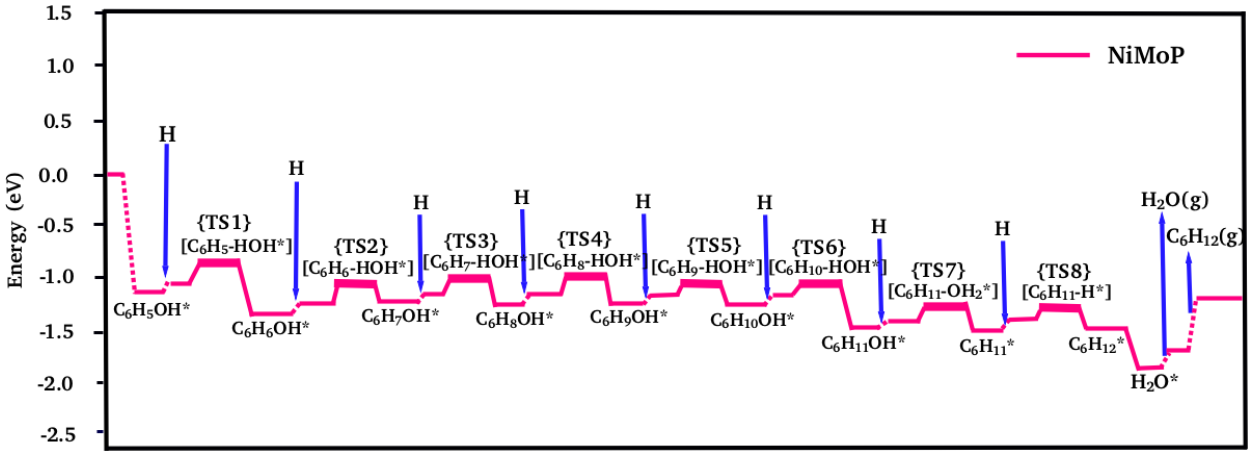

Figure S6: Reaction energetics on the (112) facet of NiMoP catalyst during RH-DO reaction.

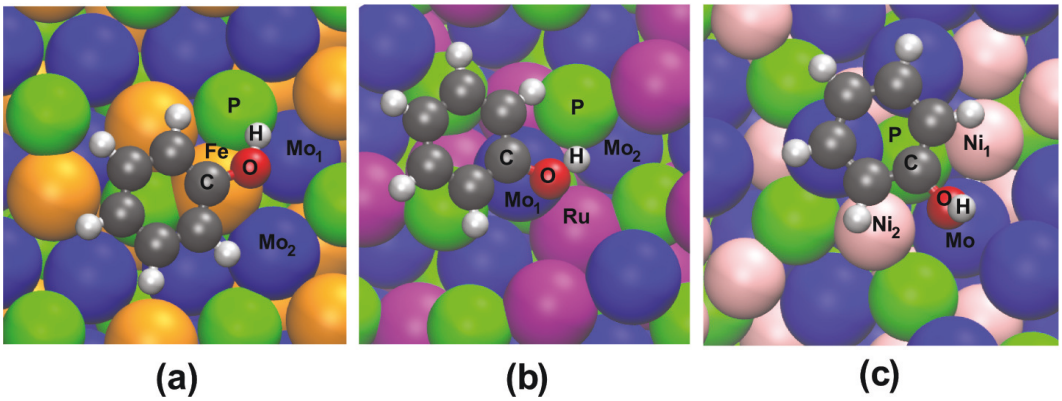

Figure S7: Atom numbering on (a) FeMoP and phenol, (b) RuMoP and phenol, (c) NiMoP and phenol systems for distance measurement in Table S7.

Table S1: Lattice vector lengths (Å) of *P (2* X *2)* simulation cell of FeMoP, RuMoP, and NiMoP systems via optB88-vdW functional

system	*a*	*b*	*c*
FeMoP	11.78	12.95	29.43
RuMoP	14.32	20.75	21.99
NiMoP	13.87	24.59	21.99

Table S2: Effect of altering the k-points grid on adsorption energy (E_{AD}, eV) of phenol and activation energy barrier (E_A, eV) of C–O bond cleavage on (112) surface of FeMoP, RuMoP, and NiMoP, respectively

system	E_{AD}			E_A		
	gamma point	2 X 2 X 1	4 X 4 X 1	gamma point	2 X 2 X 1	4 X 4 X 1
FeMoP	-1.393	-1.393	-1.394	0.372	0.372	0.373
RuMoP	-1.291	-1.294	-1.296	0.484	0.482	0.482
NiMoP	-1.215	-1.212	-1.215	0.802	0.803	0.805

Table S3: Partial charges (q, |e|) on individual atom of phenol on the (112) facet of RuMoP catalyst by using different grid size (NGX, NGY, NGZ or NGXF, NGYF, NGZF) and PREC-flag

site	NG* = 80 X 108 X 120	160 X 216 X 240	80 X 108 X 120	100 X 144 X 160
	NG*F = 160 X 216 X 240	320 X 432 X 480	80 X 108 X 120	200 X 288 X 320
C_1	+0.38	+0.40	+0.39	+0.37
C_2	+0.21	+0.24	+0.20	+0.18
C_3	– 0.18	– 0.18	– 0.19	– 0.18
C_4	+0.13	+0.13	+0.13	+0.14
C_5	– 0.22	– 0.22	– 0.22	– 0.23
C_6	– 0.13	+0.14	– 0.13	+0.14
O	– 1.10	– 1.12	– 1.10	– 1.09
H	+0.77	+0.79	+0.76	+0.75

Table S4: Cell parameters (Å) of FeMoP, RuMoP, and NiMoP system using 2 X 4 X 2 supercell size via optB88-vdW functional (experimental and computational comparison)

cell parameters	**FeMoP**		**RuMoP**		**NiMoP**	
	exp.	**comp.**	**exp.**	**comp.**	**exp.**	**comp.**
a	11.84	11.75	12.07	12.06	11.72	11.65
b	14.60	14.80	15.41	15.48	23.44	23.30
c	13.56	13.48	13.88	13.88	7.40	7.33

Table S5: Effect of simulation cell size on adsorption energies (E_{AD}, eV) of phenol (C_6H_5OH) on (112) facet of FeMoP, RuMoP, and NiMoP by using optB88-vdW functional

system	E_{AD} *(P (2 X 2))*	E_{AD} *(P (4 X 4))*
FeMoP	-1.392	-1.393
RuMoP	-1.291	-1.294
NiMoP	-1.211	-1.218

Table S6: Adsorption energies (E_{AD}, eV) of phenol (C_6H_5OH) and benzene (C_6H_6) on (112) and (111) facet of NiMoP catalyst by using optB88-vdW functional

molecule	E_{AD} (112 plane)	E_{AD} (111 plane)
phenol	-1.21	-1.26
benzene	-1.40	-1.45

Table S7: Distance (d, Å) between selected atoms of phenol (C_6H_5OH) and nearby surface atoms after adsorption on (112) facet of FeMoP, RuMoP, and NiMoP catalyst by using optB88-vdW functional (see Fig. S7 for atom numbering)

system	distance	d
FeMoP	C–Fe	2.13
	O–Fe	2.10
	O–Mo_1	3.16
	O–Mo_2	3.12
	O–P	2.40
	H–Fe	2.52
	H–Mo_1	2.94
	H–P	1.75
RuMoP	C–Ru	4.26
	C–Mo_1	2.5
	O–Ru	3.26
	O–Mo_1	2.27
	O–Mo_2	4.42
	O–P	3.02
	H–Ru	3.45
	H–Mo_1	2.66
	H–Mo_2	4.02
	H–P	2.51
NiMoP	C–Mo_1	4.58
	O–Ni_1	3.98
	O–Ni_2	3.73
	O–Mo	4.32
	O–P	4.9
	H–Ni_1	4.7
	H–Ni_2	4.68
	H–P	4.9

Table S8: Adsorption energies (E_{AD}, eV) of H on top of Fe, Ru, Ni, Mo, P atoms and in between two neighboring atoms of (112) facet by using optB88-vdW functional

atom type	E_{AD}
Fe	– 0.11
Ru	– 0.07
Ni	– 0.09
Mo	– 0.18
P	– 0.02
Fe–Mo	– 0.16
Ru–Mo	– 0.12
Ni–Mo	– 0.12
Fe–P	– 0.08
Ru–P	– 0.06
Ni–P	– 0.08
Mo–P	– 0.10

Table S9: Activation energy barriers (E_A, eV) of main elementary reaction steps involved in DDO reaction mechanism for phenol on (112) facet of FeMoP, RuMoP, and NiMoP catalyst for different DFT functionals

reaction steps	**FeMoP**		**RuMoP**		**NiMoP**	
	optB88-vdW	**PW91**	**optB88-vdW**	**PW91**	**optB88-vdW**	**PW91**
C-O cleavage	0.37	0.39	0.48	0.54	0.8	0.98
ring rotation	0.15	0.11	0.21	0.18	0.28	0.27
C-H formation	0.24	0.26	0.28	0.33	0.89	1.1

Table S10: Partial charges (q, |e|) on individual atom of phenol in gas phase and on the (111) facet of NiMoP catalyst

atom	gas phase	NiMoP
C_1	+0.39	+0.66
C_2	+0.06	+0.04
C_3	– 0.12	– 0.11
C_4	+0.002	+0.02
C_5	– 0.09	– 0.12
C_6	– 0.12	+0.04
O	– 1.16	– 1.14
H	+0.66	+0.64

Table S11: Activation energy barriers (E_A, eV) of main elementary reaction steps involved in DDO reaction mechanism for (112) and (111) facet of NiMoP catalyst by using optB88-vdW functional

reaction step	(112) plane	(111) plane
C-O cleavage	0.8	0.77
ring rotation	0.28	0.28
C-H formation	0.89	0.88

Table S12: Activation energy barriers (E_A, eV) of main elementary reaction steps involved in RH-DO reaction mechanism for phenol (C_6H_5OH) on (112) and (111) facet of NiMoP catalyst by using optB88-vdW functional

reaction step	(112) plane	(111) plane
C_1–H formation	0.21	0.17
C_2–H formation	0.12	0.09
C_3–H formation	0.04	0.05
C_4–H formation	0.08	0.05
C_5–H formation	0.12	0.1
C_6–H formation	0.07	0.05
C_6–O cleavage	0.14	0.12